

# Phase diagrams of confined square lattice links

EJ Janse van Rensburg<sup>1†</sup> & E Orlandini<sup>2‡</sup>

<sup>1</sup>Department of Mathematics and Statistics, York University, Toronto, Ontario M3J 1P3, Canada

<sup>2</sup>Dipartimento di Fisica e Astronomia “Galileo Galilei”, Università degli studi di Padova, 8 - 35131 Padova, Italia

E-mail: †rensburg@yorku.ca, ‡orlandini@pd.infn.it

6 January 2022

**Abstract.** We study by Monte Carlo simulations and scaling analysis two models of pairs of confined and dense ring polymers in two dimensions. The pair of ring polymers are modelled by squared lattice polygons confined within a square cavity and they are placed in relation to each other to be either unlinked or linked in the plane. The observed rich phase diagrams of the two models reveal several equilibrium phases separated by first order and continuous phase boundaries whose critical nature depend on this reciprocal placements. We estimate numerically the critical exponents associated with the phase boundaries and with the multicritical points where first order and continuous phase boundaries meet.

*Keywords:* Linked square lattice polygons, Parallel GARM, Multiple Markov Chain Monte Carlo, Phase boundaries, Multicritical points

Submitted to: *J Phys A: Math Theor*

PACS numbers: 82.35.Lr, 82.35.Gh, 61.25.Hq

AMS classification scheme numbers: 82B41, 82B23, 65C05

## 1. Introduction

Entanglement is an important factor determining the physical properties of polymers and biopolymers [2, 6, 7, 22]. Knotting and linking of polymers aspects of their entanglement and have been studied extensively [10, 31, 32] in lattice models [15, 21, 22, 28], also in confining spaces [26], or when adsorbed [35], or when the polymer is beyond the theta transition in the collapsed or dense phase [29, 33]. It is now known that knotting is suppressed in a lattice polygon stretched in one direction, or stretched by a force [18, 19], but enhanced when the polygon is compressed in a confining space [26]. It is also known that other thermodynamic quantities, such as pressure, is a function of knotting [16], while recent studies of compressed lattice knots show that osmotic

pressure for finite length polymers is a function of knotting [17] (see reference [8] for results for linear compressed lattice polymers).

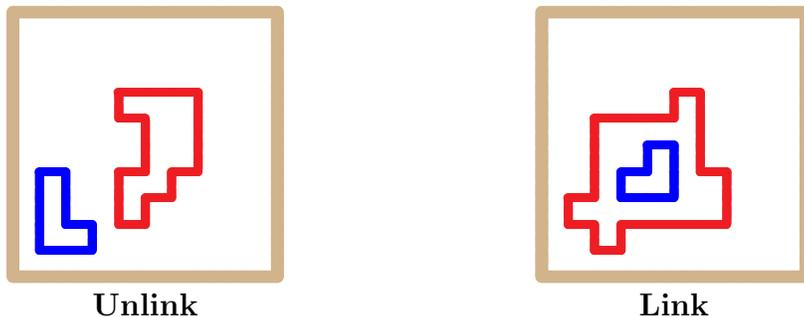


Figure 1: *Lattice models of the unlinked and linked pairs of lattice polygons in a confining square of side-length  $L$ .*

In this paper we determine the phase diagrams of a model of a pair of dense ring polymers in the plane and confined to a cavity (a convex region). The model consists of two square lattice polygons placed inside a confining square in two topologically distinct ways. The splittable placement is called the *unlinked* case, and the unsplitable placement the *linked* case (see figure 1). The lattice polygons are compressed by the confining square and so are models of dense ring polymers in two dimensions [5] (for example, ring polymers adsorbed on a surface and freely fluctuating within a cavity).

If the two polygons in figure 1 are labelled by 1 and 2, such that the outer polygon in the linked case carries label 1, then the partition functions of the two models are given by

$$\mathcal{U}_L(\alpha, \beta) = \sum_{n_1, n_2} u_L(n_1, n_2) e^{\alpha n_1} e^{\beta n_2}, \quad (1)$$

$$\mathcal{L}_L(\alpha, \beta) = \sum_{n_1, n_2} \ell_L(n_1, n_2) e^{\alpha n_1} e^{\beta n_2}. \quad (2)$$

Here,  $n_1$  and  $n_2$  are the lengths of polygons 1 and 2 respectively while the number of conformations (states) of two unlinked and linked polygons in a confining square of sidelength  $L$  and area  $L^2$  lattice sites are denoted  $u_L(n_1, n_2)$  and  $\ell_L(n_1, n_2)$ , respectively. The parameters  $(\alpha, \beta)$  are related to the chemical potentials of the monomers (vertices) along the polygons. If  $\alpha \ll 0$  and  $\beta \ll 0$  then short polygons dominate the partition functions. This corresponds to a phase of short polygons exploring the area of the confining square, and we call this the *empty phase*. If either  $\alpha \gg 0$  or  $\beta \gg 0$ , or both, then the partition functions are dominated by one or two long polygons filling the square, and the model is in a *dense phase*.

If one considers our models as  $L \times L$  systems with sites either occupied or vacant subject to topological constraints (so that the occupied sites form a pair of lattice polygons), then the (canonical) free energies of the two models are defined by

$$f_L(\alpha, \beta) = \frac{1}{L^2} \log \mathcal{U}_L(\alpha, \beta), \quad \text{and} \quad (3)$$

$$g_L(\alpha, \beta) = \frac{1}{L^2} \log \mathcal{L}_L(\alpha, \beta). \quad (4)$$

If the parameters  $(\alpha, \beta)$  are considered to be chemical potentials of vertices along the polygons, then  $f_L$  and  $g_L$  are the corresponding grand potentials of the models, and their first and second order derivatives are the concentrations and variances of the concentrations, respectively. In this paper we shall refer to  $f_L$  and  $g_L$  as *free energies*, but to their derivatives as *mean concentrations* and *variances* (of the mean concentrations). Notice that  $f_L$  and  $g_L$  are analytic functions of  $(\alpha, \beta)$ , and so phase boundaries will only exist in the  $L \rightarrow \infty$  limit. In small finite systems, finite size effects may be important, and phase boundaries are normally seen as peaks in the variances of concentrations, or as sharp changes in the concentrations. In this paper we are able to choose  $L$  large enough that in some cases free energies can be fitted to (non-analytic) absolute value functions, concentrations are approximately step functions, and the variances of concentrations have sharp spikes when crossing phase boundaries.

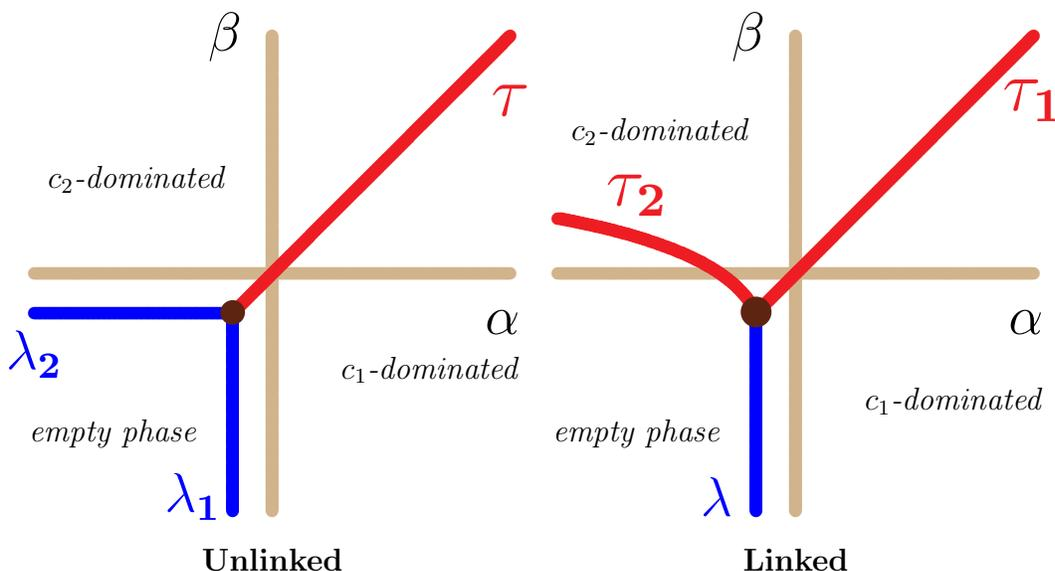


Figure 2: The phase diagrams of the unlinked (left) and linked (right) models as determined in this paper. In the unlinked model the multicritical point is located at  $(\alpha_c, \alpha_c)$ , where  $\alpha_c = -\log \mu_2$  in the  $L \rightarrow \infty$  limit (and  $\mu_2$  is the growth constant of square lattice polygons [11–13]). The location  $(\alpha_c, \beta_c)$  of the multicritical point in the linked model is more difficult to determine, where again  $\alpha = -\log \mu_2$  in limit as  $L \rightarrow \infty$ . The phase boundaries  $(\lambda_1, \lambda_2)$  in the unlinked model, and  $\lambda$  in the linked model are continuous transitions, while the  $\tau$  phase boundaries in both models are first order transitions. These phase boundaries separate empty phases from dense phase, namely a  $c_1$ -dominated phase when the first polygon (or the outer polygon in the linked model) is dense in the confining square, or a  $c_2$ -dominated phase when the second (or the inner polygon in the linked model) is dense in the confining square.

Our finite size data show that the phase diagrams of these models each include a multicritical point where three phase boundaries meet. In the unlinked model the multicritical point is the nexus of two continuous and one first order phase boundary, while in the linked model, it is the meeting point of one continuous and two first order

phase boundaries, as shown in figure 2. The locations of the multicritical points are obtained by examining the polygon generating function  $P(t)$  given by

$$P(t) = \sum_{n=0}^{\infty} p_n t^n, \quad (5)$$

where  $p_n$  is the number of square lattice polygons of length  $n$ . The radius of convergence of  $P(t)$  is  $t_c = 1/\mu_2$  [11–13] (where  $\mu_2$  is the growth constant of square lattice self-avoiding walks), so that if  $L = \infty$ , then the two polygons contributing to the partition function in equation (1) become independent and the locations of the critical lines  $\lambda_1$  and  $\lambda_2$  are along vertical and horizontal lines with  $\alpha_c = \beta_c = -\log \mu_2$ . Similarly, the location of the critical line  $\lambda$  in the linked model is along the vertical line with  $\alpha_c = -\log \mu_2$  since for  $\beta < -\log \mu_2$  the inner polygon is short and the outer polygon can expand when  $\alpha > -\log \mu_2$ .

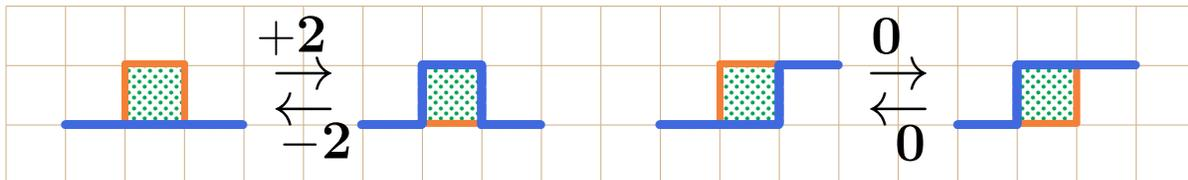


Figure 3: The BFACF elementary moves in the square lattice [1, 3]. On the left is the positive move (left to right), and the negative move (right to left). On the right is the neutral move.

In this paper our aim is to examine the phase diagrams in figure 2 numerically by simulating a  $20 \times 20$  system using Monte Carlo methods. Our data show that this finite size system is large enough to enable us to determine the phase diagram of the system with good accuracy, and to obtain reasonable estimates of the critical exponents associated with each phase boundary.

Sampling self-avoiding walks or polygons in a dense phase is a notoriously difficult numerical problem [34] but for the unlinked model a parallel implementation [4] of the GAS algorithm [20] proved effective. In the linked model we instead used the GARM [30] algorithm after the GAS algorithm failed to converge. These algorithms were implemented with BFACF elementary moves [1, 3], (see figure 3) to approximately enumerate states in the models giving estimates of  $u_L(n_1, n_2)$  and  $\ell_L(n_1, n_2)$  in equations (1) and (2). Convergence in the linked model was improved dramatically by including the neutral (total length preserving) move shown in figure 4, in addition to the standard BFACF elementary moves. Additionally, we used a multiple Markov Chain [34] implementation of the BFACF algorithm [1, 3] to sample metric and other properties of the polygons across phase boundaries to further examine the nature of the transitions shown in figure 2.

In the next section we review the critical behaviour in the phase diagrams in figure 2, before we discuss our numerical results, and examine the behaviour of several observables in these models.

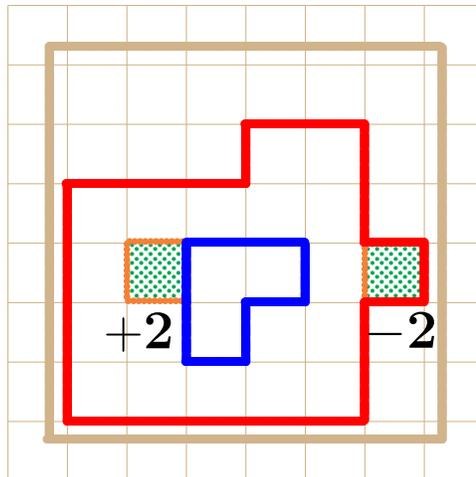


Figure 4: A neutral move on the pair of polygons in the linked model consisting of a positive (+2) move on the inner polygon, and a negative (-2) move on the outer polygon. The overall length of the two polygons remains unchanged, but they exchange edges to increase and decrease their lengths respectively.

## 2. Criticality in models of unlinked and linked dense polygons

It is not known that the thermodynamic limits (in the  $L \rightarrow \infty$  limit) exist in our models (the methods of references [24] and [14] can be used to show that some models, similar to those in figure 1, have thermodynamic limits). Assuming existence of the thermodynamic limits, define

$$v(\alpha, \beta) = \lim_{L \rightarrow \infty} f_L(\alpha, \beta), \quad \text{and} \quad (6)$$

$$\omega(\alpha, \beta) = \lim_{L \rightarrow \infty} g_L(\alpha, \beta). \quad (7)$$

These are the limiting free energies of the models, and we use the theory in reference [23] to determine the nature of the transitions along the critical lines in figure 2.

Along an axis in the phase diagram, parametrized by  $t$  and crossing a critical curve at  $t = t_c$  (see figure 5), the singular part of  $v(\alpha, \beta)$ , denoted by  $v_s(\alpha, \beta)$ , is expected to exhibit powerlaw behaviour given by

$$v_s(\alpha, \beta) \sim \begin{cases} |t - t_c|^{2-\alpha_s}, & \text{if } t \rightarrow t_c^-; \\ |t - t_c|^{2-\alpha'_s}, & \text{if } t \rightarrow t_c^+, \end{cases} \quad (8)$$

where  $\alpha_s$  and  $\alpha'_s$  are critical exponents characteristic of the transition. Similar expressions hold for the limiting free energy  $\omega(\alpha, \beta)$  of the linked model.

The functions  $v(\alpha, \beta)$  and  $\omega(\alpha, \beta)$  are approximated by  $f_L(\alpha, \beta)$  and  $g_L(\alpha, \beta)$  in equation (3) when  $L$  is finite. In this case there are finite size corrections to scaling which modifies equation (5) by introducing a *finite size* crossover exponent  $\phi_s$ . For large  $L$  the finite size corrections are small and are confined to a region close to the critical point. In this case it may be possible to extract critical exponents directly from numerical data. In this paper we are able to do this for  $L = 20$ , where our data suggest that the free energies  $f_L$  and  $g_L$  or their derivatives are closely modelled by absolute

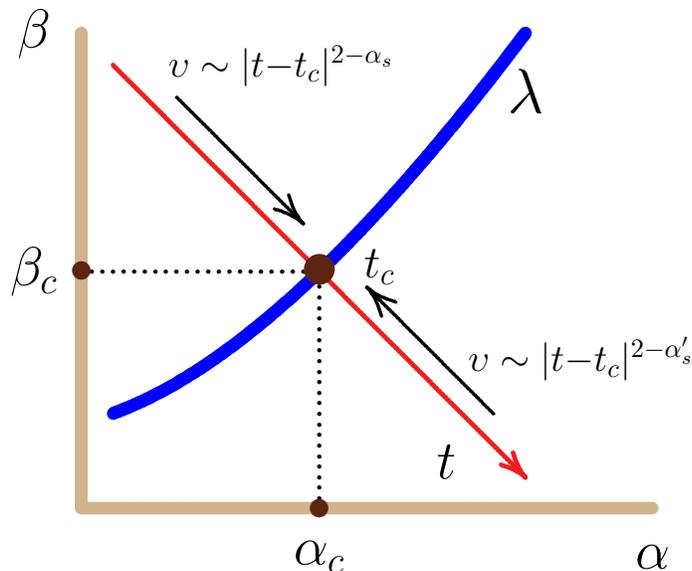


Figure 5: A schematic drawing of the transverse scaling axis crossing a phase boundary when  $t = t_c$  in the phase diagram of the unlinked or linked models. The free energy  $v(\alpha, \beta)$  is singular when  $t = t_c$ . If the transition is continuous, then there are critical exponents  $(\alpha_s, \alpha'_s)$  such that  $v(\alpha, \beta) \sim |t - t_c|^{2-\alpha_s}$  as  $t \rightarrow t_c^-$  and  $v(\alpha, \beta) \sim |t - t_c|^{2-\alpha'_s}$  as  $t \rightarrow t_c^+$ .

value or step functions, or closely follow singular behaviour given by figure (8) or its derivatives outside small finite size regions.

The phase diagrams in figure 2 include multicritical points where curves of first order and continuous transitions meet. This is shown schematically in figure 6, where a curve of first order transitions ( $\tau$ ) meets a curve of continuous transitions ( $\lambda$ ) at the *tricritical point*  $(\alpha_c, \beta_c)$ . Approaching the tricritical point along the  $\tau$  phase boundary, the singular part of  $v(\alpha, \beta)$  scales as

$$v_s(\alpha, \beta) \sim |t - t_c|^{2-\alpha_u}, \quad (9)$$

where  $t$  is the coordinate of a scaling axis along  $\tau$ . Transverse to the  $\lambda$  phase boundary at the multicritical point,

$$v_s(\alpha, \beta) \sim |s - s_c|^{2-\alpha_t}, \quad (10)$$

where  $s$  is the coordinate of the transverse scaling axis. Since  $v(\alpha, \beta)$  is a function of two variables, consistency of these scaling laws requires that there exists a *crossover exponent*  $\phi$  and scaling function  $F$  such that  $F(x) \sim x^{2-\alpha_u}$  and

$$\begin{aligned} v_s(\alpha, \beta) &\sim |s - s_c|^{2-\alpha_t} F(|s - s_c|^{-\phi} |t - t_c|) \\ &= |t - t_c|^{2-\alpha_u} (|s - s_c|^{-(2-\alpha_t)/(2-\alpha_u)} |t - t_c|)^{\alpha_u-2} \\ &\quad \times F(|s - s_c|^{-\phi} |t - t_c|) \\ &= |t - t_c|^{2-\alpha_u} F_1(|s - s_c|^{-\phi} |t - t_c|), \end{aligned} \quad (11)$$

where  $F_1(x) = x^{2-\alpha_u} F(x)$  and provided that the crossover exponent is given by

$$\phi = \frac{2-\alpha_t}{2-\alpha_u}. \quad (12)$$

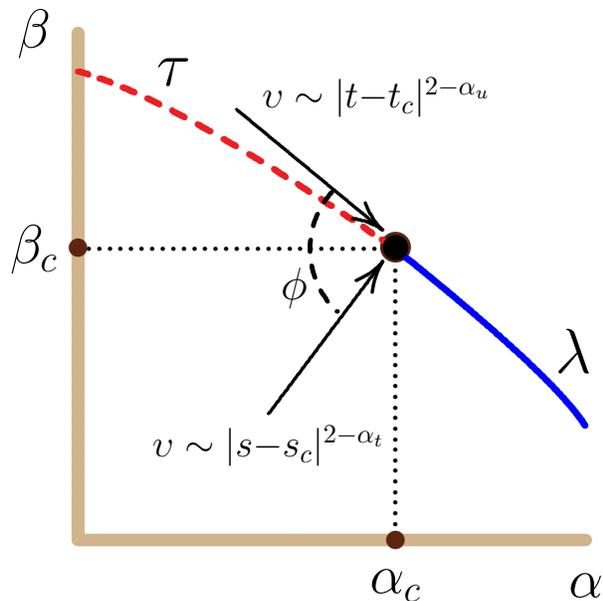


Figure 6: A tricritical point where a critical curve of first order transitions ( $\tau$ ) meets a line of continuous transitions ( $\lambda$ ). Approaching the tricritical point along  $\tau$  the free energy scales as  $v(\alpha, \beta) \sim |t - t_c|^{2 - \alpha_u}$ , where  $t$  is a coordinate along  $\tau$ . Along a second axis through the tricritical point and transverse to  $\lambda$ , the free energy scales as  $v(\alpha, \beta) \sim |s - s_c|^{2 - \alpha_t}$ , where  $s$  is a coordinate transverse to  $\lambda$ . The scaling of  $v(\alpha, \beta)$  close to the tricritical point is consistent provided that there exists a crossover exponent  $\phi$  relating to the exponents  $\alpha_u$  and  $\alpha_t$  by  $\phi = (2 - \alpha_t)/(2 - \alpha_u)$ .

Similar expressions hold for  $w(\alpha, \beta)$  of the linked model, with its exponents  $\alpha_u$ ,  $\alpha_t$  and crossover exponent  $\phi$ .

In our models the phase diagrams of the both the unlinked and linked models will be shown to include a multicritical point, generalising tricritical scaling as shown in figure 6 by the introduction of additional crossover exponents relating scaling along first order and continuous phase boundaries. In figure 7 we show the case where two continuous phase boundaries  $\lambda_1$  and  $\lambda_2$  meet a curve of first phase transitions  $\tau$  in a multicritical point. In this case there are crossover behaviour on either side of the  $\tau$  phase boundary, and each of the  $\lambda_1$  and  $\lambda_2$  phase boundaries. On each side a crossover exponent  $\phi_1$  and  $\phi_2$  controls crossover scaling. We shall show that the phase boundary of the unlinked model has the geometry shown in figure 7, albeit symmetric so that  $\phi_1 = \phi_2$  (as shown in figure 2). The phase diagram of the linked model, in contrast has a multicritical point where two curves  $\tau_1$  and  $\tau_2$  of first order phase transitions meet a curve  $\lambda$  of continuous transitions. In this model the situation is similar to that shown in figure 7, but now with scaling along parallel axes on each of the  $\tau_1$  and  $\tau_2$  phase boundaries, and transverse to the  $\lambda$  phase boundary. This gives crossover scaling between  $\tau_1$  and  $\lambda$  with crossover exponent  $\phi_1$ , and similarly between  $\tau_2$  and  $\lambda$  with crossover exponent  $\phi_2$ .

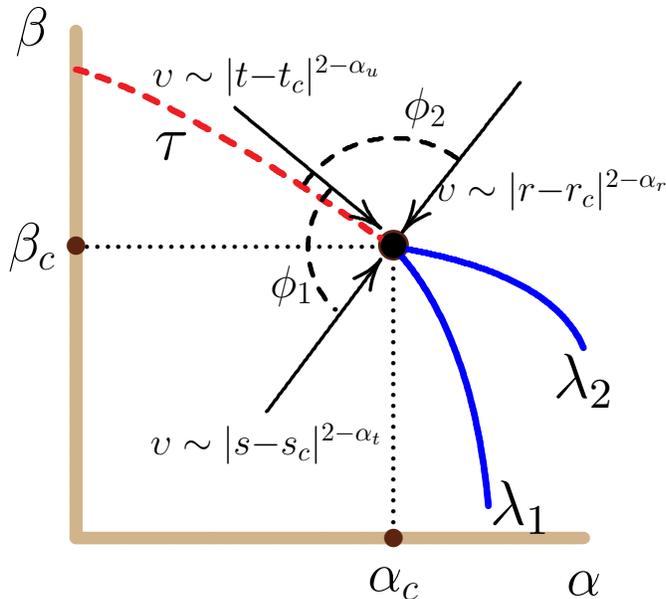


Figure 7: A multicritical point where a critical curve of first order transitions ( $\tau$ ) meets two curves of continuous transitions ( $\lambda_1$  and  $\lambda_2$ ). Approaching the multicritical point along  $\tau$  the free energy scales as  $v(\alpha, \beta) \sim |t - t_c|^{2 - \alpha_u}$ , where  $t$  is a coordinate along  $\tau$ . Along a second axis through the multicritical point and transverse to  $\lambda_1$ , the free energy scales as  $v(\alpha, \beta) \sim |s - s_c|^{2 - \alpha_t}$ , where  $s$  is a coordinate transverse to  $\lambda_1$ . The scaling of  $v(\alpha, \beta)$  between  $\tau$  and  $\lambda_1$  close to the multicritical point is consistent provided that there exists a crossover exponent  $\phi_1$  relating the exponents  $\alpha_u$  and  $\alpha_t$  by  $\phi_1 = (2 - \alpha_t)/(2 - \alpha_u)$ . Similarly, transverse to  $\lambda_2$  the free energy scales as  $v(\alpha, \beta) \sim |r - r_c|^{2 - \alpha_r}$ , where  $r$  is a coordinate transverse to  $\lambda_2$ . This defines a crossover exponent  $\phi_2$  relating the exponents  $\alpha_u$  and  $\alpha_r$  by  $\phi_2 = (2 - \alpha_r)/(2 - \alpha_u)$ .

### 3. Numerical results

Simulations on the unlinked model with  $L = 20$  were performed using the GAS algorithm [20] with BFACF elementary moves [1,3] (figure 3). A parallel implementation (similar to the implementation of PERM in reference [4]) using 8 threads and shared data structures was run for 2,000 started sequences (or *tours*) each of length  $10^7$  iterations. This amounts to a total of  $1.6 \times 10^{11}$  sampled configurations (iterations). The simulation converged in reasonable time to very stable estimates of  $u_L(n_1, n_2)$  (see equation (1)). The linked model proved far more difficult and did not converge successfully, notable because the GAS algorithm failed to effectively sample states with  $n_1 < n_2$  (that is, a short outer polygon with enclosed area filled with a long inner polygon as expected in the  $c_2$ -dominated phase). Using the GARM algorithm instead, implemented with BFACF elementary moves and an additional neutral move (see figure 4), proved effective, and a parallel implementation with 12 parallel threads, sampling along GARM sequences for a total of  $12 \times 4.03 \times 10^5$  tours, converged in reasonable time (see reference [4]).

The GAS and GARM algorithms are approximate enumeration algorithms producing estimates of the microcanonical partitions  $u_L(n_1, n_2)$  and  $\ell_L(n_1, n_2)$  in

equations (1) and (2). This gives estimates of the free energies  $f_L$  and  $g_L$  (equations (3) and (4)) and in the event that  $L$  is large enough, we obtain accurate approximations to the limiting free energies  $\nu(\alpha, \beta)$  and  $\omega(\alpha, \beta)$  in equations (6) and (7). Our simulations show that  $L = 20$  are sufficiently large, and that it will be challenging to perform simulations for  $L > 20$ , in particular for the linked model.

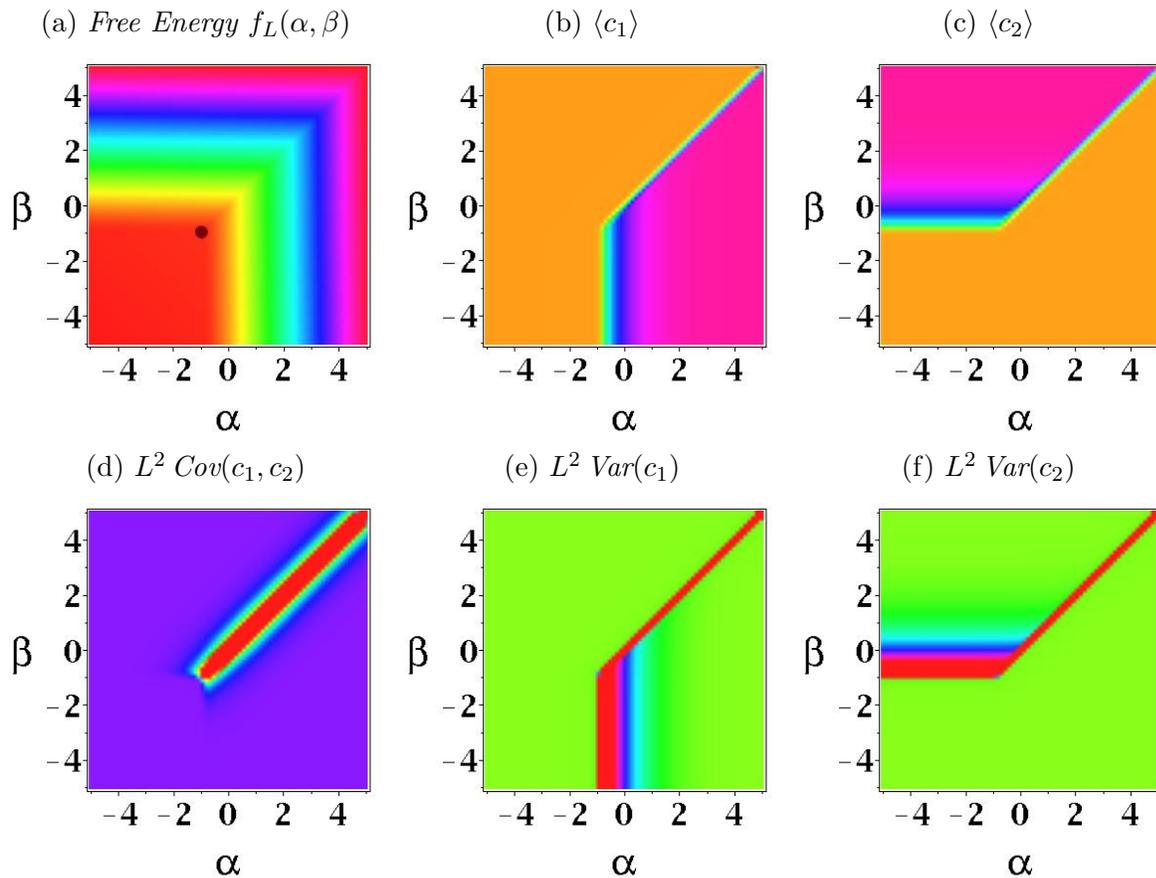


Figure 8: The free energy  $f_L(\alpha, \beta)$  of the unlinked model for  $L = 20$  (top left), and its first and second derivatives. Proceeding clockwise from the top middle, the energies  $\langle c_1 \rangle$  and  $\langle c_2 \rangle$ , the specific heats (variances)  $\text{Var}(c_2)$  and  $\text{Var}(c_1)$ , and the covariance of  $c_1$  and  $c_2$   $\text{Cov}(c_1, c_2)$ . The concentrations  $c_1$  and  $c_2$  are negatively correlated, and shows a sharp transition along the main diagonal for  $\alpha = \beta > \alpha_c$ . The location of the multicritical point in the model is denoted by a bullet in (a).

### 3.1. The phase diagram of two unlinked confined square lattice polygons

In figure 8(a) a density plot of  $f_L(\alpha, \beta)$  for  $L = 20$  is shown, with the left bottom colour low, and the right and top colours high. The free energy shows clear signs of transitions, and this is also confirmed by plotting other observables related to the first and second derivatives of  $f_L(\alpha, \beta)$ . The mean concentrations of vertices in each polygon are related to the mean lengths of the polygons by

$$\langle c_1 \rangle = \langle n_1 \rangle / L^2 = \frac{d}{d\alpha} f_L(\alpha, \beta). \quad (13)$$

The concentration of the second polygon is similarly given by  $\langle c_2 \rangle = \langle n_2 \rangle / L^2 = \frac{d}{d\beta} f_L(\alpha, \beta)$ . Density plots of  $\langle c_1 \rangle$  and  $\langle c_2 \rangle$  are shown in figures 8(b) and (c). These plots show rapid change in the mean concentrations of one, or both, the polygons when phase boundaries are crossed.

The variance of the concentration  $c_1$  is given by

$$\text{Var}(c_1) = \frac{1}{L^4} \text{Var}(n_1) = \frac{1}{L^2} \frac{\partial^2}{\partial \alpha^2} f_L(\alpha, \beta) \quad (14)$$

and in figure 8(e) a density plot of  $L^2 \text{Var}(c_1)$  is shown, and this shows a phase boundary (where  $\text{Var}(c_1)$  is large) separating phases where  $\langle c_1 \rangle$  is small from a phase where  $\langle c_1 \rangle$  is large. A similar plot of  $L^2 \text{Var}(c_2)$  is shown in figure 8(f) for the concentration  $c_2$  of the second polygon. The covariance of  $c_1$  and  $c_2$  is given by

$$\begin{aligned} \text{Cov}(c_1, c_2) &= \frac{1}{L^4} (\langle n_1 n_2 \rangle - \langle n_1 \rangle \langle n_2 \rangle) \\ &= \frac{1}{L^2} \frac{\partial^2}{\partial \alpha \partial \beta} f_L(\alpha, \beta), \end{aligned} \quad (15)$$

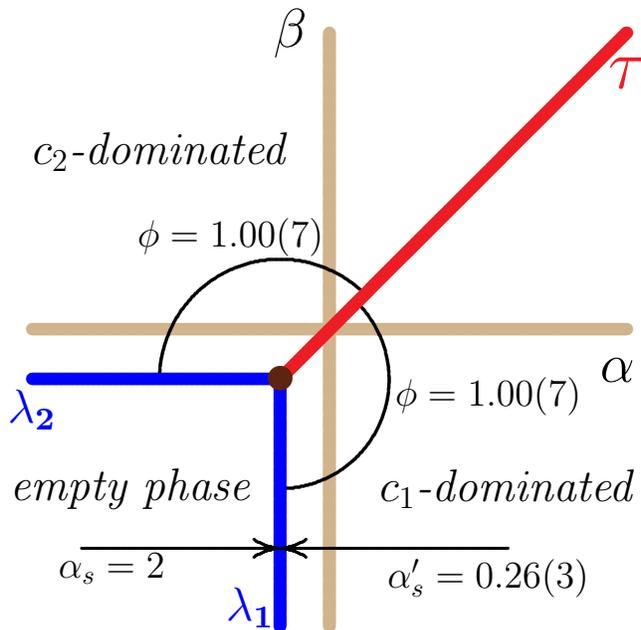
and  $L^2 \text{Cov}(c_1, c_2)$  is plotted in figure 8(d). The covariance is small negative in most of the plot, but spikes to large negative along a phase boundary which runs along the diagonal with points  $(\alpha, \beta)$  where  $\alpha = \beta > \alpha_c$  and starting in a multicritical point  $(\alpha_c, \alpha_c)$  since the phase diagram is symmetric under exchange  $\alpha \leftrightarrow \beta$ .

These results numerically confirm the phase diagram of the unlinked model shown in figures 2 and figure 9. The multicritical point  $(\alpha_c, \alpha_c)$  is situated at the meeting of three phase boundaries. The phase transition along the main diagonal, denoted by  $\tau$ , is a line of transitions starting in the multicritical point running into the first quadrant. Up to numerical accuracy, above and to the left of  $\tau$  the free energy is only a function of  $\beta$ , and to the right and below it, only a function of  $\alpha$ . This shows that  $\tau$  is a first order phase boundary separating a phase where  $\langle c_2 \rangle$  is large from a phase where  $\langle c_1 \rangle$  is large. These are the *c<sub>2</sub>-dominated* and *c<sub>1</sub>-dominated* phases, respectively.

Two additional phase boundaries are meeting at the multicritical point, namely a line of transitions  $\lambda_1$  running vertically into the multicritical point and a line of transitions  $\lambda_2$  running horizontally into the multicritical point. The vertical phase boundary separates a phase where both  $\langle c_1 \rangle$  and  $\langle c_2 \rangle$  are small (this is the *empty phase*) from a *c<sub>1</sub>-dominated* phase. Similarly, the horizontal phase boundary separates the empty phase from a *c<sub>2</sub>-dominated* phase.

Note that, since  $f_L(\alpha, \beta)$  is an analytic function of  $(\alpha, \beta)$ , these phases and phase boundaries exist only in the  $L \rightarrow \infty$  limit. In our data the phase boundaries manifest themselves as peaks in the variances or sharp changes in the mean concentrations. The location of the multicritical point is obtained by observing that the radius of convergence of the polygon partition function  $P(t)$  in equation (2) is  $t_c = 1/\mu_2$ , so that if  $L = \infty$ , then the two polygons contributing to equation (3) become independent and the critical points are determined by the polygon generating function. This gives  $\alpha_c = \beta_c = -\log \mu_2 \approx -0.97$ .

*3.1.1. Critical scaling in the unlinked model* **The  $\tau$  phase boundary:** In figure 10 the free energy, mean concentrations and variances for  $L = 20$  are plotted as a function



**Unlinked model phase diagram**

Figure 9: Crossover exponents between  $\tau$  and the  $\lambda_1$  and  $\lambda_2$  critical curves around the multicritical point in the phase diagrams of the unlinked models. This phase diagram is symmetric over the main diagonal, so that the crossover exponents  $\phi$  on either side have the same value.

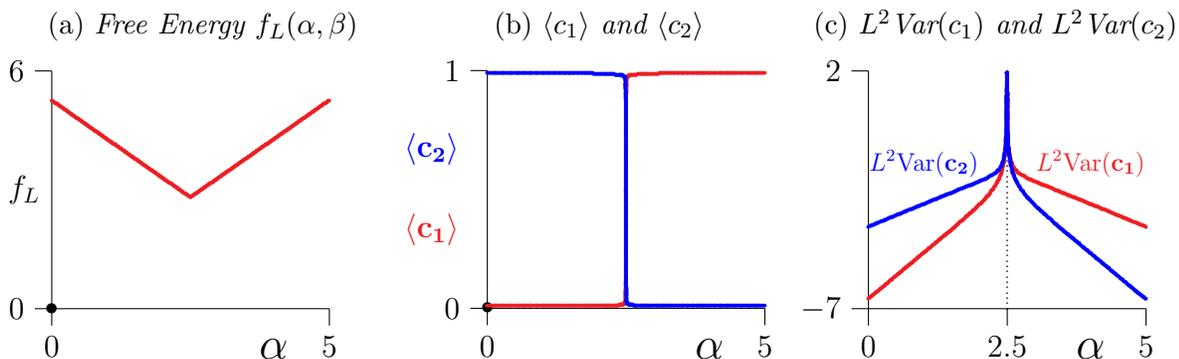


Figure 10: The free energy, mean concentrations and variances of the unlinked model as a function of  $\alpha$  along the line crossing the  $\tau$  phase boundary between the points  $(0, 5)$  to  $(5, 0)$  in the phase diagram in figure 9. These data were calculated for  $L = 20$ , but shows that the free energy is to numerical accuracy an absolute function, non-analytic on the  $\tau$  phase boundary. The mean concentrations  $\langle c_1 \rangle$  and  $\langle c_2 \rangle$  are approximately step functions at the critical line, while the variances, plotted on a logarithm vertical scale, develop sharp spikes at the critical point, while having very small values (less than  $10^{-3}$ ) away from the critical point.

of  $\alpha$  from the point  $(0, 5)$  along the line segment to  $(0, 5)$ . The critical point (where the  $\tau$  phase boundary is crossed) corresponds to  $\alpha = 2.5$ , and this is seen in the plot of the

free energy  $f_L$  in figure 10(a). The phase transition along the  $\tau$  phase boundary is a first order transition to numerical accuracy, as the limiting free energy in equation (6) is accurately approximated by  $f_L$  for  $L = 20$ , and  $f_L$  can be directly modelled by an absolutely value function. Indeed, using the 5-parameter model

$$v(\alpha, 5-\alpha) = a_0 + a_1 |\alpha - a_c|^{2-\alpha_s} + a_2 (\alpha - a_c)^2 \quad (16)$$

a nonlinear fit (done using the *NonlinearFit* function in Maple [25]) can be performed to obtain estimates of the exponent  $2-\alpha_s$ . If we first ignore the quadratic term (by putting  $a_2 = 0$ ) to obtain

$$v(\alpha, 5-\alpha) \approx 2.810 + 0.975 |\alpha - 2.498|^{1.003}. \quad (17)$$

Repeating the fit with  $a_2$  as an additional parameter gives instead

$$\begin{aligned} v(\alpha, 5-\alpha) \approx & 2.810 + 0.976 |\alpha - 2.499|^{1.006} \\ & + 0.00153 (\alpha - 2.499)^2. \end{aligned} \quad (18)$$

Notice the very small coefficient of the quadratic term, showing that the free energy is very closely approximated by the absolute value term. These fits give the critical point at  $a_c = 2.498$  (compared to its exact value 2.5 by symmetry) and the estimate of the exponent  $2-\alpha_s = 2-\alpha'_s \approx 1.003$  (see equation (5)). Notice that the coefficient of the quadratic term is very small, showing that even in this finite size model, with  $L = 20$ , the free energy is well approximated by a non-analytic function, showing a sharp transition at the critical point.

As in figure 5 one may now estimate the scaling exponent associated with the  $\tau$  phase boundary. Taking as error bar the difference in the estimates in equations (17) and (18),

$$2 - \alpha_s = 2 - \alpha'_s = 1.003 \pm 0.003. \quad (19)$$

This is consistent with the transition across the  $\tau$  phase boundary being first order.

**The  $\lambda_1$  and  $\lambda_2$  phase boundaries:** Next, consider the transition across the  $\lambda_1$  phase boundary by calculating the free energy along the line segment from  $(-5, -2)$  to  $(5, -2)$ . The results are plotted in figure 11 as a function of  $\alpha$ . The graphs in figure 11(b) of the concentrations  $\langle c_1 \rangle$  and  $\langle c_2 \rangle$  show that the transition across the  $\lambda_1$  phase boundary does not have a step-like increase, unlike the case for the  $\tau$  phase boundary. Since the  $\lambda_1$  phase boundary in figure 9 is a vertical line and  $\alpha_c \approx -0.97$ , the transition across  $\lambda_1$  is expected to occur at  $\alpha_c$ , and our data are consistent with this. The critical exponent associated with the transition is defined by equation (8), and since the free energy  $f_L$  in figure 11 is (up to numerical accuracy) a constant for  $\alpha < \alpha_c$  we conclude that  $2-\alpha_s = 0$  along the  $\lambda_1$  phase boundary as  $\alpha \rightarrow \alpha_c^-$ .

If  $\alpha > \alpha_c$  the concentration  $\langle c_1 \rangle$  increases sharply at the critical point (as shown in figure 11(b)). As  $\alpha$  increases in size, one expects that the first polygon becomes dense and then fills the confining square, and  $\langle c_1 \rangle \rightarrow 1$ . In view of equation (8),

$$\langle c_1 \rangle \sim |\alpha - \alpha_c|^{1-\alpha'_s}, \text{ for } \alpha \rightarrow \alpha_c^+ \text{ and } \beta = -2. \quad (20)$$

The exponent can be estimated by plotting  $\log \langle c_1 \rangle / \log |\alpha - \alpha_c|$  as a function of  $1 / \log |\alpha - \alpha_c|$ . This is improved if we subtract from  $\langle c_1 \rangle$  its (small but non-zero) value

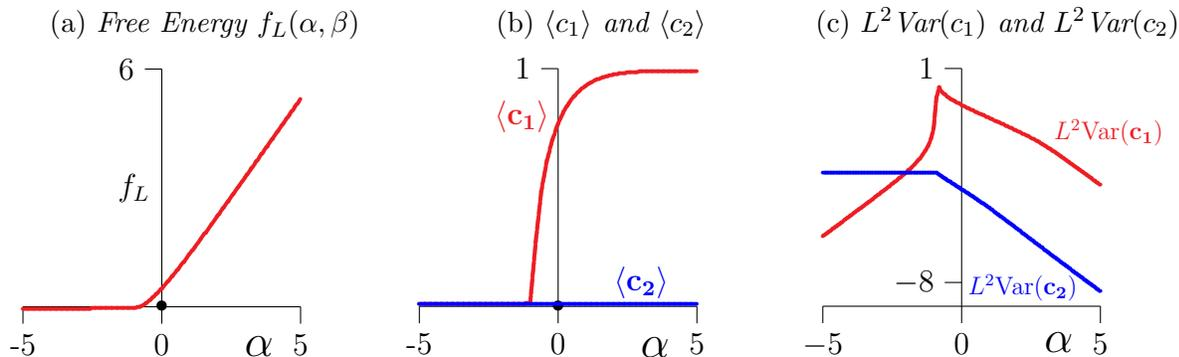


Figure 11: The free energy, mean concentrations and variances of the unlinked model as a function of  $\alpha$  along the line from the point  $(-5, -2)$  to  $(5, -2)$  crossing  $\lambda_1$  in the phase diagram in figure 9. In this figure  $L = 20$ . The free energy shows a transition at approximately  $\alpha_c \approx -\log \mu_2 \approx -0.97$ , and this is seen in the behaviour of the mean concentration  $\langle c_1 \rangle$ . Our analysis strongly suggests that this transition between the empty and the  $c_1$ -dominated phase is continuous. Notice that  $\langle c_2 \rangle$  appears to be unchanged in the middle graph, but if the logarithm of variances are plotted, then  $\text{Var}(c_2)$  is singular at the critical point, going from constant into a steady decline. Since our model is symmetric in  $\{c_1, c_2\}$ , these graphs will be unchanged (except with  $c_1$  and  $c_2$  interchanged) if instead these quantities are calculated along the line from  $(-2, -5)$  to  $(-2, 5)$  which crosses over the phase boundary  $\lambda_2$  separating the empty and the  $c_2$ -dominated phases.

$\langle c_1 \rangle|_{crit}$  at  $\alpha = \alpha_c$ , to zero it at the critical point. This removes a background term due to the finite size of our model since  $L = 20$ . Defining

$$\log \langle c_1 \rangle_s = \log(\langle c_1 \rangle - \langle c_1 \rangle|_{crit}) \quad (21)$$

we get the model

$$\begin{aligned} \gamma &= \log \langle c_1 \rangle_s / \log |\alpha - \alpha_c| \\ &= (1 - \alpha'_s) + C / \log |\alpha - \alpha_c| + \dots \end{aligned} \quad (22)$$

Choosing  $\alpha_c = -0.97$  and then plotting  $\gamma$  as a function of  $1/\log |\alpha - \alpha_c|$  for  $-0.95 \leq \alpha \leq 0$  gives the graph in figure 12. This graph is almost a straight line, except at points where  $\alpha$  approaches  $\alpha_c$ . Fitting a linear function in  $1/\log |\alpha - \alpha_c|$  to the graph gives the estimate  $1 - \alpha'_s \approx 0.545$ , and fitting a quadratic instead gives  $1 - \alpha'_s \approx 0.516$ . The difference in these two estimates is taken as a confidence interval in the estimate.

On the empty phase side of  $\lambda_1$  the free energy is constant to numerical accuracy, and so one expects  $\alpha_s = 2$ . Taken together,

$$\alpha_s = 2 \quad \text{and} \quad \alpha'_s \approx 0.45 \pm 0.03 \quad (23)$$

along the  $\lambda_1$  phase boundary. The stated error bar on  $\alpha'_s$  is the standard deviation of the estimates in the table above.

Thus, the transitions along the  $\lambda_1$  phase boundary has exponents  $2 - \alpha_s = 0$  and  $2 - \alpha'_s = 1.55(3)$  in equation (8). Since the model is symmetric in  $\{c_1, c_2\}$ , these results will be the same if instead the  $\lambda_2$  phase boundary between the empty and  $c_2$ -dominated phases is crossed.

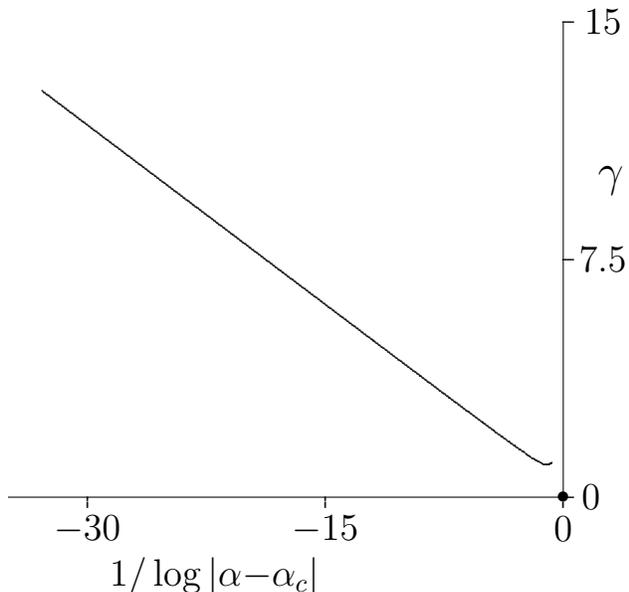


Figure 12: Plotting  $\gamma = \log(\langle c_1 \rangle - \langle c_1 \rangle_{crit}) / \log |\alpha - \alpha_c|$  as a function of  $1 / \log |\alpha - \alpha_c|$  for the unlinked model along a line segment in the  $c_1$ -dominated phase starting in the  $\lambda_1$  phase boundary with  $\beta = -2$ . In this graph  $-0.9 \leq \alpha < 0$ .

**Scaling around the multicritical point:** Scaling axes through the multicritical point are set up consistent with figure 7. The parallel scaling axis (parallel to the  $\tau$ -phase boundary) runs along the  $\tau$  phase boundary on the main diagonal from  $(-5, -5)$  to  $(5, 5)$ . The transverse axis (transverse to the  $\tau$ -line) runs along the  $\lambda_2$  phase boundary and crosses the multicritical point into the  $c_1$ -dominated phase. Similarly, a second transverse axis runs along the  $\lambda_1$  phase boundary into the  $c_2$ -dominated phase.

Estimates of the free energy  $f_L$  and its derivatives are plotted for  $L = 20$  on the axes through the multicritical point in figure 13. The three top panels show results along the parallel scaling axis, while the bottom panels display results along the transverse scaling axis running along  $\lambda_2$  and crossing into the  $c_1$ -dominated phase.

Since the phase diagram is symmetric about the main diagonal in the  $\alpha\beta$ -plane, and since the free energy is not a function of  $\beta$  in the  $c_1$ -dominated phase, and of  $\alpha$  in the  $c_2$ -dominated phase, it follows that the scaling of  $\langle c_1 \rangle$  and  $\langle c_2 \rangle$  along these axes is the same as given in equation (20) with  $\alpha'_s$  and  $\alpha_s$  having the values in equation (23). This follows by symmetry, since  $f_L(\alpha, \alpha_c) = f_L(\alpha, \beta)$  for any  $\beta < \alpha_c$ , and  $f_L(\alpha, \alpha) = f_L(\alpha, \alpha_c)$  in the dense phases (that is, for  $\alpha > \alpha_c$ ). Thus, it follows that the exponents  $\alpha_u$  and  $\alpha_t$  in equations (9) and (10) have the same values as in equation (23), namely

$$\alpha_u = \alpha_t \approx 0.45 \pm 0.03. \quad (24)$$

By equation (12), the crossover exponent in this model is  $\phi = 1$ . Taking into account the uncertainty of the estimate in equation (24), the estimate of the crossover exponent of the unlinked model is given by

$$\phi = 1.00 \pm 0.04. \quad (25)$$

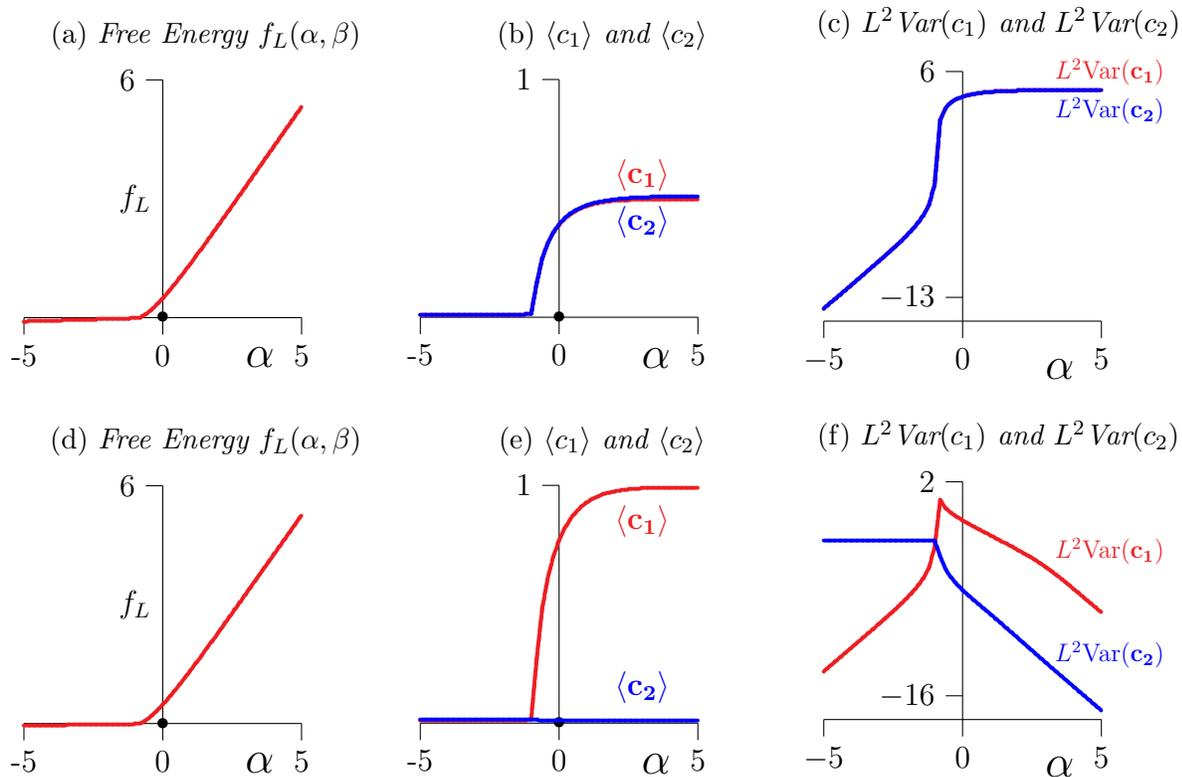


Figure 13: *Top panels:* The free energy, mean concentrations and variances of the unlinked model as a function of  $\alpha = \beta$  along the line from the point  $(-5, -5)$  to  $(5, 5)$  through the multicritical point in the phase diagram in figure ???. The free energy (top left) shows a transition at approximately  $\alpha_c = \beta_c \approx -\log \mu_2 \approx -0.97$  (as also seen in the graphs of the mean concentrations  $\langle c_i \rangle$ ). These critical curves show a transition as the multicritical point is crossed into the dense phase where the polygons fill the confining square. The mean concentrations show a singular point in the free energy at the critical point, and the variances (plotted on a logarithmic scale) show a sharp increase at this point.

*Bottom panels:* The free energy, mean concentrations and variances as a function of  $\alpha$  on the line through the multicritical point and with endpoints  $(-5, \beta_c)$  and  $(5, \beta_c)$  (where  $\beta_c = -\log \mu_2 \approx -0.97$ ). These data shown a continuous transition, similar to the transition seen in figure ?? between the empty phase, and the  $c_1$ -dominated phase.

### 3.2. The phase diagram of two linked confined square lattice polygons

In figure 14(a) is a density plot of  $g_L(\alpha, \beta)$  (for  $L = 20$ ) with the left bottom colour low, and the right and top colours high. The free energy shows clear signs of phase transitions, and this is also seen in plots of the first and second derivatives of  $g_L(\alpha, \beta)$  shown in figures 14(b)-(f).

The concentrations  $\langle c_1 \rangle$  and  $\langle c_2 \rangle$  (see equation (13)) are plotted in figures 14(b) and (c). These plots show a rapid change in the mean concentration of one, or both,  $\langle c_1 \rangle$  and  $\langle c_2 \rangle$  when phase boundaries are crossed. Note that these plots are different from those in figure 8, suggesting that the different topology of this model (namely that the

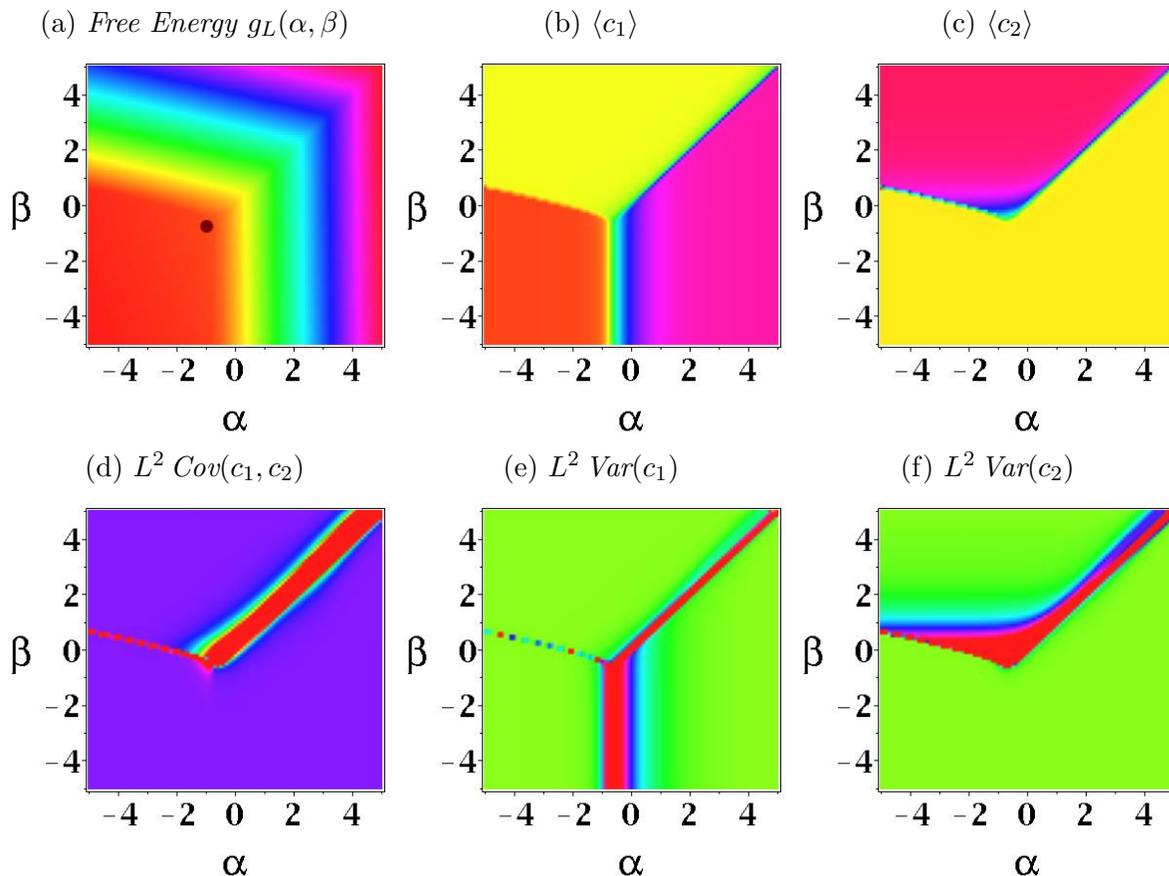


Figure 14: The free energy  $g_L(\alpha, \beta)$  of the linked model for  $L = 20$  (top left), and its first and second derivatives. Proceeding clockwise from the top middle, the mean concentrations of the outer polygon  $\langle c_1 \rangle$  and the inner polygon  $\langle c_2 \rangle$ , their variances  $Var(c_2)$  and  $Var(c_1)$ , and the covariance of  $c_1$  and  $c_2$ ,  $Cov(c_1, c_2)$ . The concentrations  $c_1$  and  $c_2$  are negatively correlated, and the covariance shows a sharp transition close to the main diagonal for  $\alpha = \beta > \alpha_c$ . In addition, a second, apparently weaker, phase change appears along a curve starting in the multicritical point and runs along a curve into the second quadrant, and a third transition runs vertically into the multicritical point from below. The approximate location of the multicritical point in the model is denoted by a bullet in (a).

two polygons are linked in  $\mathbb{R}^2$ ) has a relevant impact on its thermodynamic properties.

The variances (equation (14)) and covariance (equation (15)) are plotted in figure 14(d), (e) and (f). The covariance shows (as expected) strong negative correlations between  $c_1$  and  $c_2$  induced by the confining square, except along two phase boundaries, where the correlation is positive.  $Var(c_1)$  in figure 14(e), considered with figure 14(b), shows a phase boundary  $\tau_1$  close to or on the main diagonal for  $\alpha > \alpha_c$  and  $\beta > \beta_c$  where  $(\alpha_c, \beta_c)$  is the location of a multicritical point.

Magnifying figure 14(a) in the vicinity of the multicritical point gives the density plot in figure 15. This plot suggest that the a *curved* phase boundary  $\tau_2$  separates the empty phase from a  $c_2$ -dominated phase for large positive  $\beta$  (in this phase the

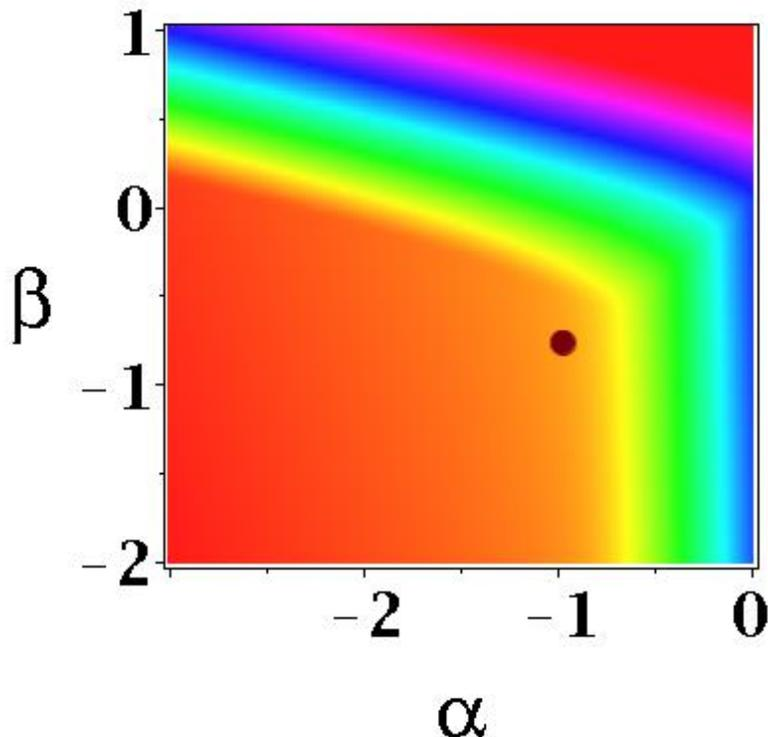


Figure 15: A density plot the free energy  $g_L(\alpha, \beta)$  of the linked model in the vicinity of the multicritical point. The location of the multicritical point is estimated to be  $(\alpha, \beta) = (-0.97, -0.77)$  and is denoted by the bullet.

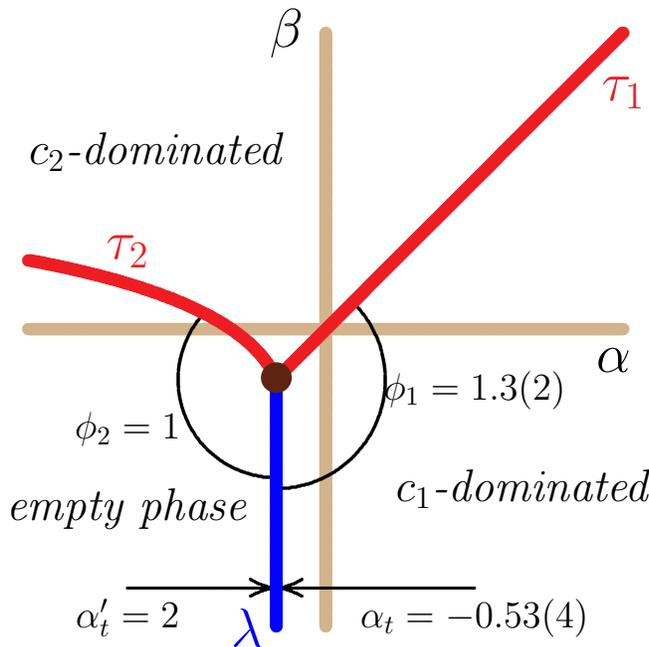
inner polygon is dense, and the outer polygon is expanded to near the perimeter of the confining square).

The rest of the phase diagram, as suggested by figures 14 and 15, is shown in figure 16. A vertical phase boundary  $\alpha = \alpha_c$  runs from the multicritical point for  $\beta < \beta_c$ . This phase boundary, denoted by  $\lambda$ , separates an empty phase, for large negative  $\alpha$  and  $\beta$ , from a  $c_1$ -dominated phase for large positive  $\alpha$ . This transition is similar to the transition across the  $\lambda_1$  phase boundary in the unlinked model, and the critical value of  $\alpha$  is given by  $\alpha_c = -\log \mu_2$  (using an argument similar to the one used for  $\lambda_1$  in the unlinked model). Crossing  $\lambda$  takes the model from its empty phase into a phase where the outer polygon is dense, while the inner polygon remains small.

Since the multicritical point  $(\alpha_c, \beta_c)$  is the intersection of the three phase boundaries  $\lambda$ ,  $\tau_1$  and  $\tau_2$ , with the  $\lambda$  phase boundary running vertically and separating the empty phase from the  $c_1$ -dominated phase, we conclude that  $\alpha_c = -\log \mu_2 \approx -0.97$ , but, as will be seen below, it appears from our numerical data that  $\beta_c > -0.97$ , although the resolution of our data was not good enough to confirm this.

To determine the trajectories of  $\tau_1$  and  $\tau_2$ , we estimated from our data sets of points along them. In the case of  $\tau_1$  a linear least squares fit using a quadratic model shows that

$$\tau_1(\alpha) \approx 0.0824 + 0.9824 \alpha + 0.00268 \alpha^2,$$



Linked model phase diagram

Figure 16: Crossover exponents between the  $\tau_1$  and  $\lambda$ , and  $\tau_2$  and  $\lambda$  critical curves around the multicritical point in the phase diagram of the linked model.

$$\text{for } \alpha > -0.97. \quad (26)$$

Since along the critical curve  $\lambda$  the value of  $\alpha = \alpha_c \approx -0.97$ , it follows that this predicts that the multicritical point appears to be close to  $(-0.97, -0.868)$ .

In the case of  $\tau_2$  a 3-parameter non-linear fit using the *NonlinearFit* function in the Statistics package of Maple17 [25] was used along points on the phase boundary. Assuming a powerlaw shape gives the trajectory

$$\tau_2(\alpha) \approx -0.6680 + 0.5184 |-0.97 - \alpha|^{0.64}, \quad \text{for } \alpha < -0.97. \quad (27)$$

This predicts that the multicritical point is close to  $(-0.97, -0.668)$ . Taking the average of this estimate, and the estimate obtained from the trajectory of the  $\tau_1$  phase boundary, gives our best estimate of the location of the multicritical point for the linked case:

$$(\alpha_c, \beta_c) \approx (-0.97, -0.77), \quad (28)$$

assuming, of course, that finite size corrections at  $L = 20$  is negligible. Note that the estimate of  $\beta_c$  is larger than the one reported for the unlinked model (namely,  $\beta_c \approx -0.97$ ). This estimate may have a large confidence interval, since numerical estimates in the vicinity of the multicritical point are strongly affected by the environment (namely, it is the intersection of three phase boundaries) and the resolution of our simulations is not good enough to determine a more accurate location.

**3.2.1. Critical scaling in the linked model** **The  $\tau_1$  phase boundary:** In the top row of figure 17 the free energy and its derivatives are plotted as a function of  $\alpha$  along the

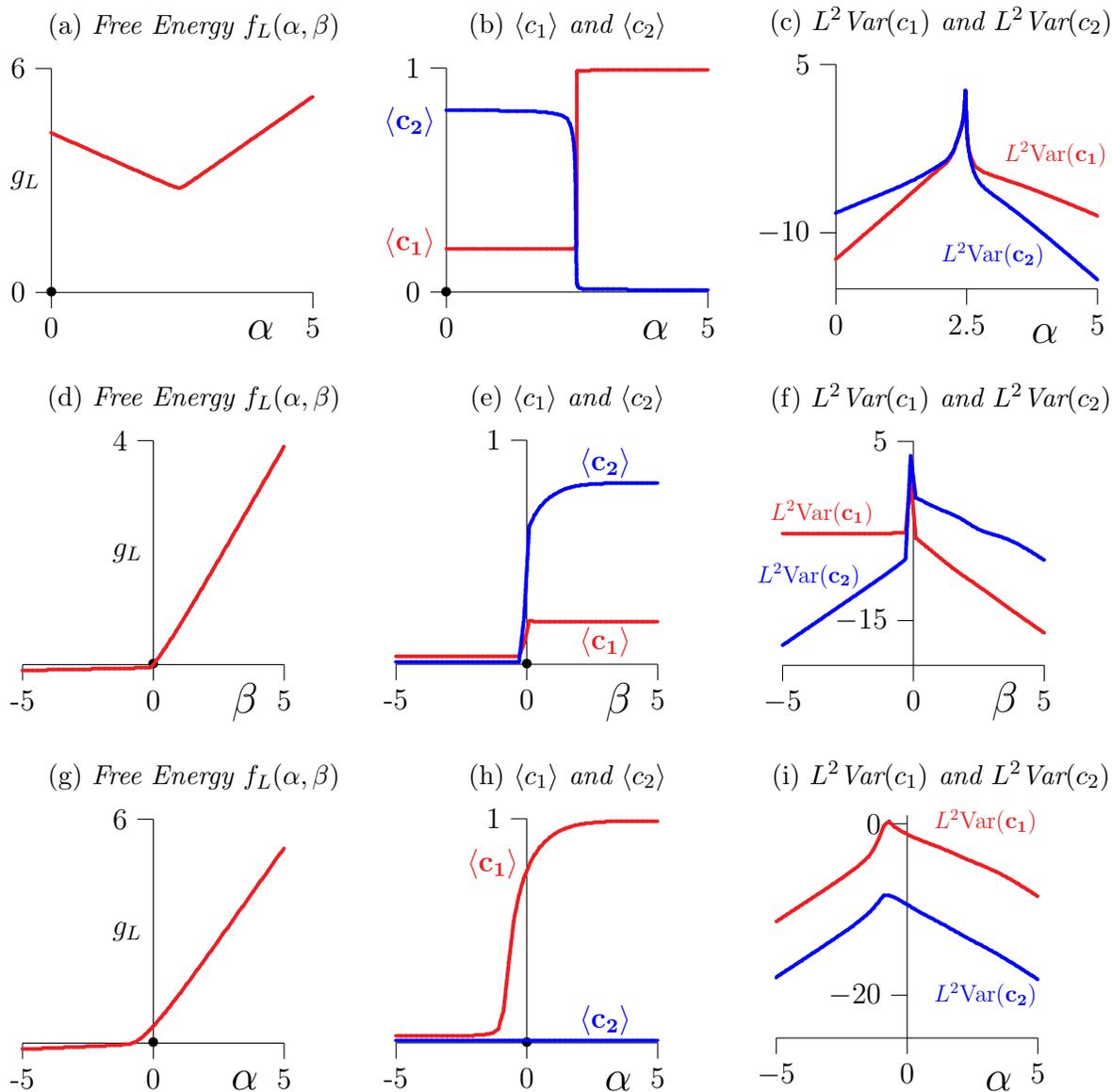


Figure 17: Top row: The free energy, mean concentrations and variances of the linked model as a function  $\alpha$  along the line segment from  $(0, 5)$  to  $(5, 0)$  across the  $\tau_1$  phase boundary. The variances are plotted on a logarithmic vertical scale.

Middle row: The free energy, mean concentrations and variances as a function of  $\beta$  on the line segment from the point  $(-2, -5)$  to the point  $(-2, 5)$  across the  $\tau_2$  phase boundary.

Bottom row: The free energy, mean concentrations and variances as a function of  $\alpha$  on the line segment across the  $\lambda$  phase boundary from  $(-5, -2)$  to  $(5, -2)$ .

line segment from  $(0, 5)$  to  $(5, 0)$  in the phase diagram. As in the unlinked model, the free energy can be fitted to an absolute value function using the model

$$w(\alpha, 5-\alpha) = a_0 + a_1 \alpha + a_2 |\alpha - \alpha_c|^{2-\alpha_s} + a_3 (\alpha - \alpha_c)^2. \quad (29)$$

The curve in figure 17(a) appears to be rotated about its minimum, and to account for

this, a linear term in  $\alpha$  was included in equation (29). A fit with  $a_3 = 0$  (so that there is no quadratic correction) gives

$$w(\alpha, 5-\alpha) \approx 2.3172 + 0.1823 \alpha + 0.7747 |\alpha - 2.4592|^{1.018}, \quad (30)$$

while including the quadratic term in the model gives

$$w(\alpha, 5-\alpha) \approx 2.3259 + 0.1819 \alpha + 0.7737 |\alpha - 2.4583|^{1.057} - 0.0124 (\alpha - 2.4583)^2. \quad (31)$$

We note again the relative small coefficient of the quadratic term, suggesting minor curvature of the  $\tau_1$  phase boundary for  $-0.97 \leq \alpha \leq 5$ . Equation (27) shows that the  $\tau_1$  phase boundary is crossed approximately at the point (2.4592, 2.5408) by the line segment from (0, 5) to (5, 0) in the phase diagram, consistent with the observation that the  $\tau_1$  phase boundary is slightly off-set from the main diagonal in the  $\alpha\beta$ -plane.

The critical exponents  $2-\alpha_s$  and  $2-\alpha'_s$  (see equation (8)) can also be read from the fits in equations (30) and (31):

$$2 - \alpha_s = 2 - \alpha'_s = 1.02 \pm 0.04. \quad (32)$$

The error bar is the absolute difference between the estimates in equations (30) and (31). These results are consistent with a first order transition along  $\tau_1$  (which is seen in the jump discontinuities in  $\langle c_1 \rangle$  and  $\langle c_2 \rangle$  shown in the top middle graph in figure 17).

**The  $\tau_2$  phase boundary:** The free energy, concentrations and variances across this phase boundary are plotted in figure 17 along a line segment from  $(-2, -5)$  to  $(-2, 5)$ . The jump discontinuities in  $\langle c_1 \rangle$  and  $\langle c_2 \rangle$  are consistent with this also being a first order transition. Fits similar to equations (30) and (31) give the approximations

$$w(-2, \beta) \approx -0.0392 + 0.4013 \beta + 0.3517 |\beta - 0.0517|^{1.059}. \quad (33)$$

and

$$w(-2, \beta) \approx -0.0188 + 0.4017 \beta + 0.3400 |\beta - 0.0567|^{1.182} - 0.0151 (\beta - 0.0567)^2. \quad (34)$$

Comparison of these fits with equation (8) give the estimated critical exponents

$$2 - \alpha_s = 2 - \alpha'_s = 1.06 \pm 0.12 \quad (35)$$

and critical point  $(-2, \tau_2(-2)) \approx (-2, -0.52(5))$  on the  $\tau_2$  phase boundary. These values are again consistent with  $\tau_2$  being a curve of first order transitions.

**The  $\lambda$  phase boundary:** The data along the  $\lambda$  phase boundary are plotted in the bottom panels of figure 17. The concentration  $\langle c_1 \rangle$  plotted in figure 17(h) is obtained from estimates along the line segment between the points  $(-5, -2)$  and  $(5, -2)$  in the phase diagram. In this graph  $\langle c_1 \rangle$  has a profile consistent with a continuous transition.

As in the unlinked model, the scaling exponent  $\alpha'_s$  in equation (8) can be estimated by plotting  $\log \langle c_1 \rangle_s / \log |\alpha - \alpha_c|$  (equation (22)) as a function of  $1/\log |\alpha - \alpha_c|$ . Plotting  $\gamma$  in equation (22) as a function of  $1/\log |\alpha - \alpha_c|$  for  $-0.95 \leq \alpha \leq 0$  gives the graph

in figure 18 . Fitting a linear function in  $1/\log |\alpha - \alpha_c|$  to the graph gives the estimate  $1 - \alpha'_s \approx 0.57$ , and fitting a quadratic instead gives  $1 - \alpha'_s \approx 0.63$ . The difference in these two estimates is taken as a confidence interval in the estimate.

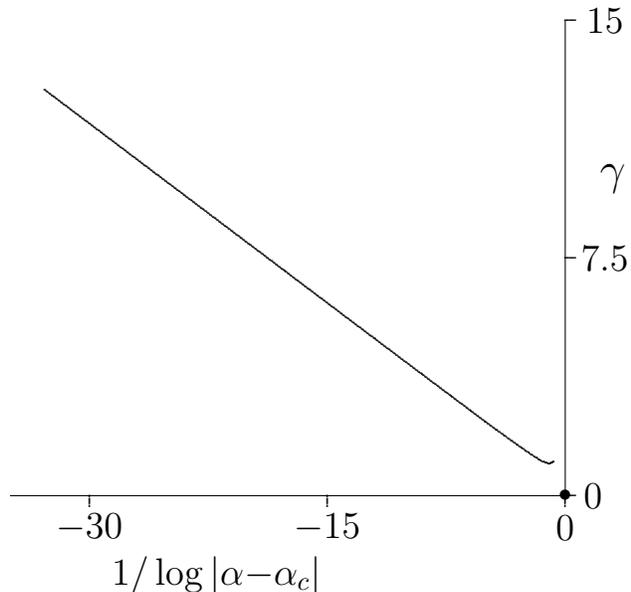


Figure 18: Plotting  $\gamma = \log(\langle c_1 \rangle - \langle c_1 \rangle_{crit}) / \log |\alpha - \alpha_c|$  as a function of  $1/\log |\alpha - \alpha_c|$  for the linked model in the  $c_1$ -dominated phase along a line segment starting in the  $\lambda$  phase boundary, with  $\beta = -2$ . In this graph  $-0.9 \leq \alpha \leq 0$ .

On the empty phase side of  $\lambda$  the free energy is constant to numerical accuracy, and so one expects  $\alpha_s = 2$ . Taken together,

$$\alpha_s = 2 \quad \text{and} \quad \alpha'_s \approx 0.43 \pm 0.06 \quad (36)$$

This shows that  $2 - \alpha_s = 0$  on the empty phase side of  $\lambda$ , and  $2 - \alpha'_s = 1.57(6)$  on the  $c_1$ -dominated phase side.

**Scaling around the multicritical point:** In the phase diagram in figure 16 a transverse scaling axis is set up to run horizontally through the multicritical point, while two parallel scaling axes are set up to run along the first phase order phase boundaries.

The free energies, mean concentrations and variances of the concentrations are plotted along the parallel and transverse scaling axes in figure 19. Along the transverse axis (shown in figure 19(h)) our data show that the concentrations remain unchanged when compared to figure 17(h). Thus, the transverse scaling exponents are the same as those found along the  $\lambda$  phase boundary given in equation (35), namely  $\alpha_t = 2$  from the  $\tau_2$  side of the phase boundary, and  $\alpha_t = 0.43(6)$  on the  $\tau_1$  side.

Since the trajectory of the  $\tau_1$  phase boundary and location of the multicritical point are not known exactly, it is more challenging to estimate the scaling exponent  $\alpha_u$ . Putting  $\ell(\alpha) = (\alpha, \tau_1(\alpha))$  and denoting the distance along  $\tau_1$  between  $\ell(\alpha_c)$  and  $\ell(\alpha)$  in the  $\alpha\beta$ -plane by  $d(\alpha_c, \alpha)$ , the exponent  $\alpha_u$  can be estimated by calculating the ratio  $\log \langle c_1 \rangle_s / \log d(\alpha_c, \alpha)$  with  $\alpha_c = -0.970$  along  $\tau_1$  (see equations (21) and (22)). By the

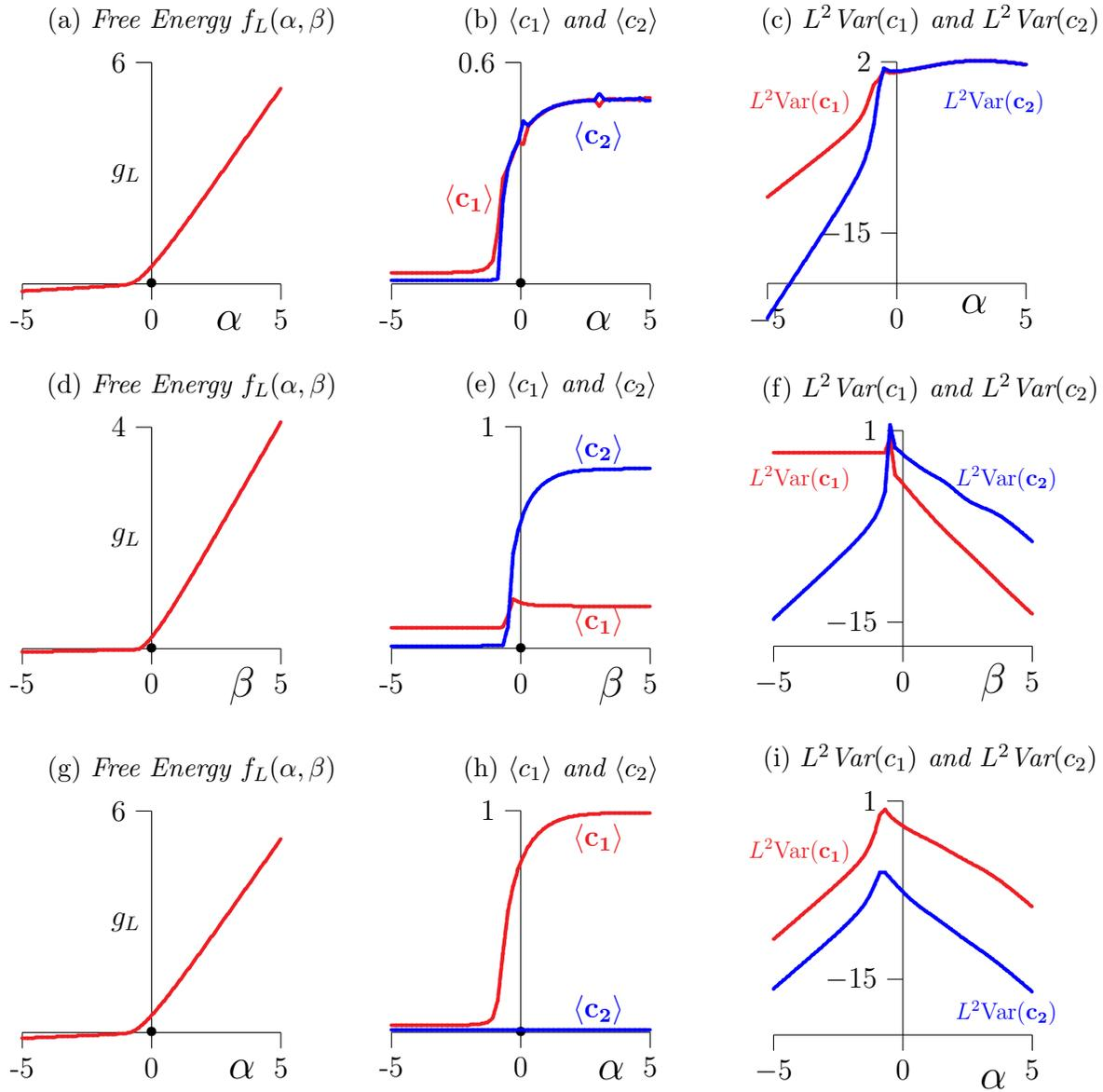


Figure 19: Top row: The free energy, mean concentrations and variances of the linked model as a function of  $\alpha$  from the empty phase and then along the  $\tau_1$  phase boundary. The variances are plotted on a logarithmic vertical scale.

Middle row: The free energy, mean concentrations and variances as a function of  $\beta$  along the  $\lambda$  phase boundary and tangent to the  $\tau_2$  phase boundary at the multicritical point. The data is plotted against  $\beta$  along the line segment from  $(\alpha_c, -5)$  to the point  $(\alpha_c, 5)$ .

Bottom row: The free energy, mean concentrations and variances as a function of  $\alpha$  transverse to the  $\lambda$  phase boundary through the multicritical point along the line segment from  $(-5, \beta_c)$  to  $(5, \beta_c)$  into the  $c_1$ -dominated phase.

same arguments leading to equation (22), we plot

$$\gamma = \log \langle c_1 \rangle_s / \log d(\alpha_c, \alpha) \quad (37)$$

as a function of  $1/\log d(\alpha_c, \alpha)$  and estimate the exponent  $1 - \alpha_u$  by a linear fit. This

gives the graph in figure 20.

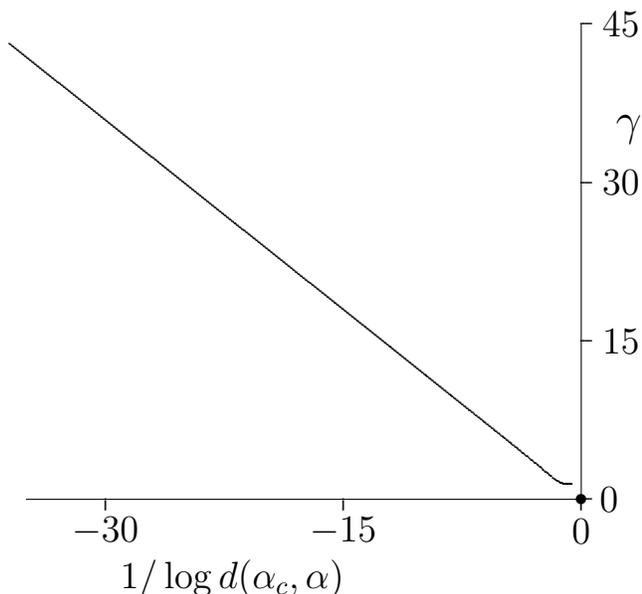


Figure 20: Plotting  $\gamma = \log(\langle c_1 \rangle - \langle c_1 \rangle|_{crit}) / \log d(\alpha_c, \alpha)$  as a function of  $1/\log d(\alpha_c, \alpha)$  for the linked model along the trajectory of the  $\tau_1$  phase boundary, starting in the multicritical point. In this graph  $-0.9 \leq \alpha \leq -0.2$ .

A linear fit to the data in figure 20 gives  $1-\alpha_u \approx 0.172$  and a quadratic fit gives  $1-\alpha_u \approx 0.242$ . Taking the difference as an error bar gives the estimate  $1-\alpha_u = 0.17 \pm 0.07$ . Thus, our estimate is

$$\alpha_u = 0.83 \pm 0.07, \quad \text{along } \tau_1. \quad (38)$$

Comparing this with the estimate of  $\alpha_t$  on the  $c_1$ -dominated phase side of the  $\lambda$  gives the estimated crossover exponent  $\phi_1 = 1.3 \pm 0.2$ , by equation (12).

Along the  $\tau_2$  phase boundary the situation is simpler. This phase boundary is between the empty phase and the  $c_2$ -dominated phase, and the free energy is continuous along  $\tau_2$ . Since the free energy in the scaling limit is a constant in the empty phase, it is also, by continuity, a constant along the  $\tau_2$  phase boundary in the scaling limit. Thus, one concludes that  $\alpha_u = 2$  along  $\tau_2$ , whereas the transverse exponent on the empty phase side of  $\lambda$  is  $\alpha_t = 2$  as well. This gives the crossover exponent  $\phi = 1$  between the  $\lambda$  and  $\tau_2$  phase boundaries.

### 3.3. Finite size effects

In the previous sections we have considered the phase diagrams for  $L = 20$ . In this section we briefly consider finite size effects in our data. We do this only for the linked model; finite size effects in the unlinked model are smaller and phase boundaries do not move with increasing  $L$ .

In figure 21(a) the concentrations  $\langle c_1 \rangle$  are plotted along a line segment as the  $\lambda$  phase boundary is crossed into the  $c_1$ -dominated phase in the linked model, for systems

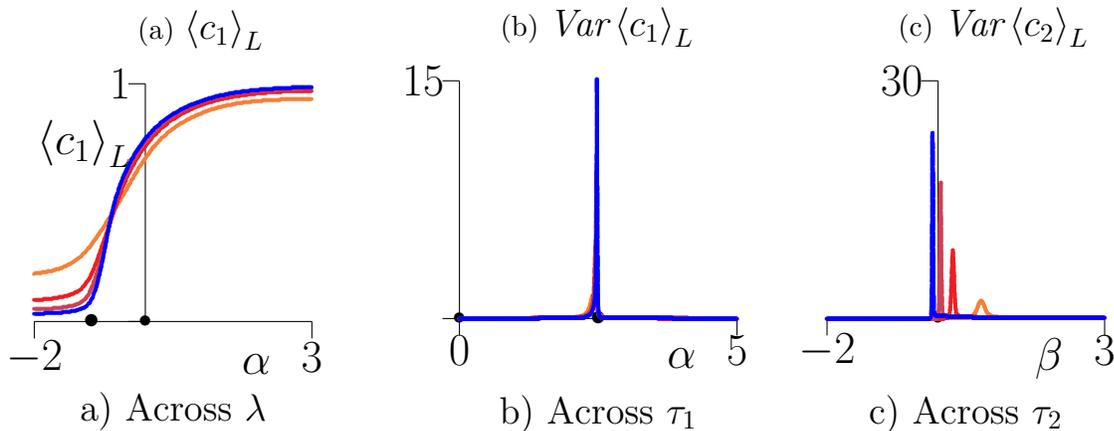


Figure 21: (a) The concentration of the outer polygon in the linked model along a line segment with  $\beta = -2$  crossing the  $\lambda$  phase boundary in the  $c_1$ -dominated phase, for system sizes  $L = 8, 12, 16$ , and  $20$ . The location of the critical point is denoted by a bullet. (b) The variance of  $\langle c_1 \rangle$  across the  $\tau_1$  phase boundary along the line segment from  $(0, 5)$  to  $(5, 0)$ . The data develop a sharp spike when the critical line is crossed, with minimal widening close to the critical point. The width decreases with increasing  $L$ . In this graph the data are plotted for system sizes  $L = 8, 12, 16$ , and  $20$ . (c) The variance of  $\langle c_2 \rangle$  as a function of  $\beta$  along the line segment from  $(-2, -2)$  to  $(-2, 3)$ . With increases  $L$  in  $\{8, 12, 16, 20\}$  the data show an increasing spike which narrows quickly in width and shifting to the left to a limiting location as  $L$  increases to infinity.

of sizes  $L = 8, 12, 16$  and  $20$ . The graphs show quick convergence towards a limiting curve with increasing  $L$ , particularly in the  $c_1$ -dominated phase. Finite size effects are most pronounced close to the critical point, and is seen in the slight upturn of the plot in figure 18 when  $\alpha$  approaches  $\alpha_c$ . We accommodated for this by fitting a linear function to data, while discarding data close to the critical point.

Figure 21(b) is a graph of the variance  $\text{Var}(c_1)$  plotted along a line segment from  $(0, 5)$  to  $(5, 0)$  crossing the  $\tau_1$  phase boundary, for  $L = 8, 12, 16$  and  $20$ . These curves all spike sharply when  $\tau_1$  is crossed at  $\alpha \approx 2.48$ . The heights of the spikes increase by almost doubling as  $L$  increments by 4. Finite size effects can be seen in the slight broadening at the base of the spikes, and this broadening decreases with increasing  $L$ .

The variance  $\text{Var}(c_2)$  plotted along a vertical line from  $(-2, -2)$  to  $(-2, 3)$  across the  $\tau_2$  phase boundary is shown in figure 21(c) for  $L = 8, 12, 16$  and  $20$ . For each  $L$  this shows a spike roughly twice the height of the spikes in figure 21(b). With increasing  $L$  the spikes move, towards the left, but with decreasing increments. This shows that the location of the  $\tau_2$  phase boundary remains uncertain, but also that it should converge to a limiting curve of first order transitions along which  $\text{Var}(c_2)$  is divergent.

#### 4. Characterising the transitions

The nature of transitions across phase boundaries in these models can also be explored by defining and tracking order parameters and metric observables as the system is

taken through a transition. Numerical estimates of order parameters were obtained by sampling the models using a Multiple Markov Chain Metropolis algorithm [9, 27, 34] implementing BFACF elementary moves (see figure 3) [1, 3] on each polygon. In our implementation we sampled along 50 Markov chains (performing  $10^5$  iterations along each sequence) along lines in the  $\alpha\beta$ -plane. Apart from tracking the lengths  $n_1$  and  $n_2$  of the polygons, these simulations also collected data on the number of nearest neighbour contacts  $k_1$  and  $k_2$  in each polygon (these are *self-contacts*), as well as the number of nearest neighbour contacts  $k_m$  between polygons (these are *mutual contacts*).

Let  $w_L(n_1, n_2; k_1, k_2, k_m)$  be the number of conformations of the unlinked or linked model in a square of side-length  $L$ , of lengths  $n_1$  and  $n_2$  respectively, with  $k_1$  self-contacts in the first polygon,  $k_2$  in the second, and  $k_m$  mutual contacts. The mean *density of self-contacts* of the first polygon is defined by

$$\langle k_1/L^2 \rangle = \frac{\sum_{\substack{n_1, n_2 \\ k_1, k_2, k_M}} (k_1/L^2) u_L(n_1, n_2; k_1, k_2, k_M) e^{\alpha n_1} e^{\beta n_2}}{\sum_{\substack{n_1, n_2 \\ k_1, k_2, k_M}} u_L(n_1, n_2; k_1, k_2, k_M) e^{\alpha n_1} e^{\beta n_2}}. \quad (39)$$

The densities  $\langle k_2/L^2 \rangle$  of self-contacts in the second polygon, and  $\langle k_m/L^2 \rangle$  of mutual contacts, are defined similarly.

We sampled data on metric observables, namely the mean square radius of gyration of the first polygon (a function of  $(\alpha, \beta)$ ),  $\langle r_1^2 \rangle$ , and the corresponding quantity for the second polygon,  $\langle r_2^2 \rangle$ . Moreover we look at the mean distance or separation between the centres-of-mass of the two polygons,  $\langle d_{cm} \rangle$ .

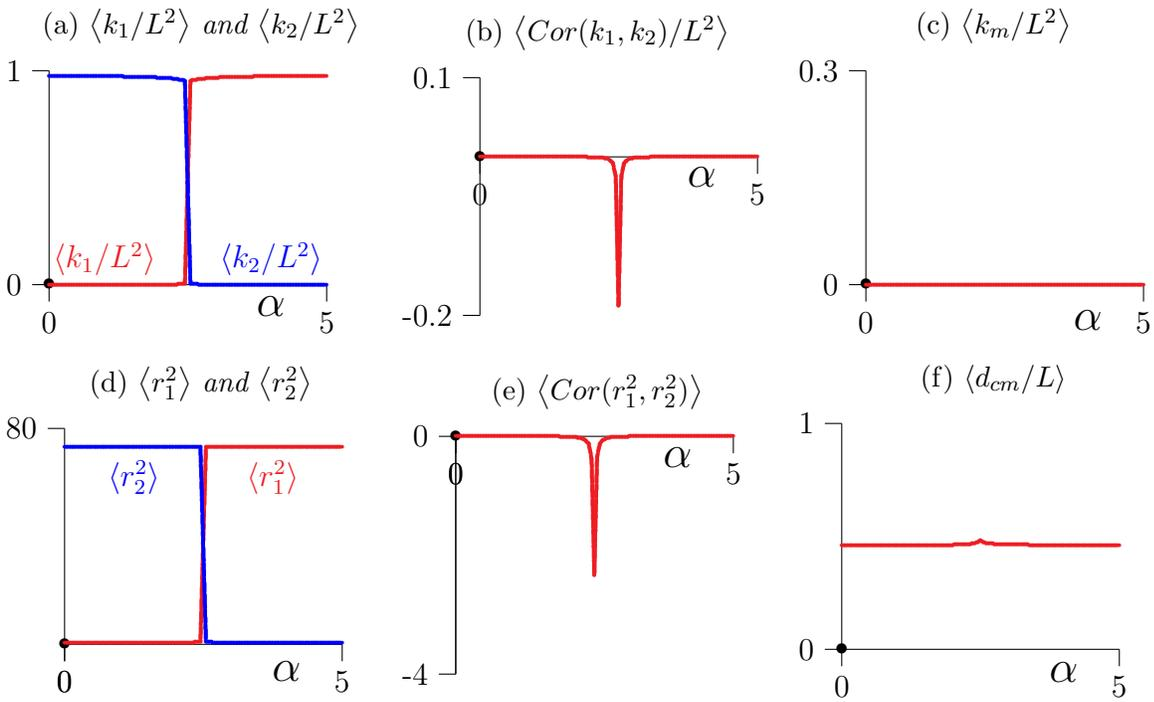
In addition to these quantities, the correlations  $Cor(k_1, k_2) = \langle k_1 k_2 \rangle - \langle k_1 \rangle \langle k_2 \rangle$  (between self-contacts in the polygons), and  $Cor(r_1^2, r_2^2) = \langle r_1^2 r_2^2 \rangle - \langle r_1^2 \rangle \langle r_2^2 \rangle$  (between the square radii of gyration of the two polygons) were calculated.

In figure 22 we show thermodynamic and metric data estimates along the line segment with endpoints  $(0, 5)$  and  $(5, 0)$  in the phase diagram for the unlinked model (figure 10) and the linked model (figure 17). This line crosses the  $\tau$  phase boundary in the unlinked model, and the  $\tau_1$  phase boundary in the linked model. The results for the unlinked case are shown in figures 22(a)-(f), while the results for the linked model are shown in figures 22(g)-(l).

The results in both models are consistent with a first order transition as the phase boundaries ( $\tau$  or  $\tau_1$ , respectively) are crossed. There are sharp discontinuities in the mean number of self-contacts in both models, as well as in the metric quantities. The correlations show sharp peaks at the locations of the transitions. Figure 22(j) indicates that the outer polygon in the linked model is inflated by the inner polygon in the  $c_2$ -dominated phase, and expands in the  $c_1$ -dominated phase to compress the inner polygon to a very small size.

In figure 23 the estimated mean quantities are plotted as the linked model is taken through the  $\tau_2$  phase boundary. The results are consistent with those in figure 17(d)-(f), showing a strong first order character as the inner polygon inflates the outer polygon when the model is taken from the empty phase into the  $c_2$ -dominated phase in figure

Unlinked from  $(0, 5)$  to  $(5, 0)$  across  $\tau$ :



Linked from  $(0, 5)$  to  $(5, 0)$  across  $\tau_1$ :

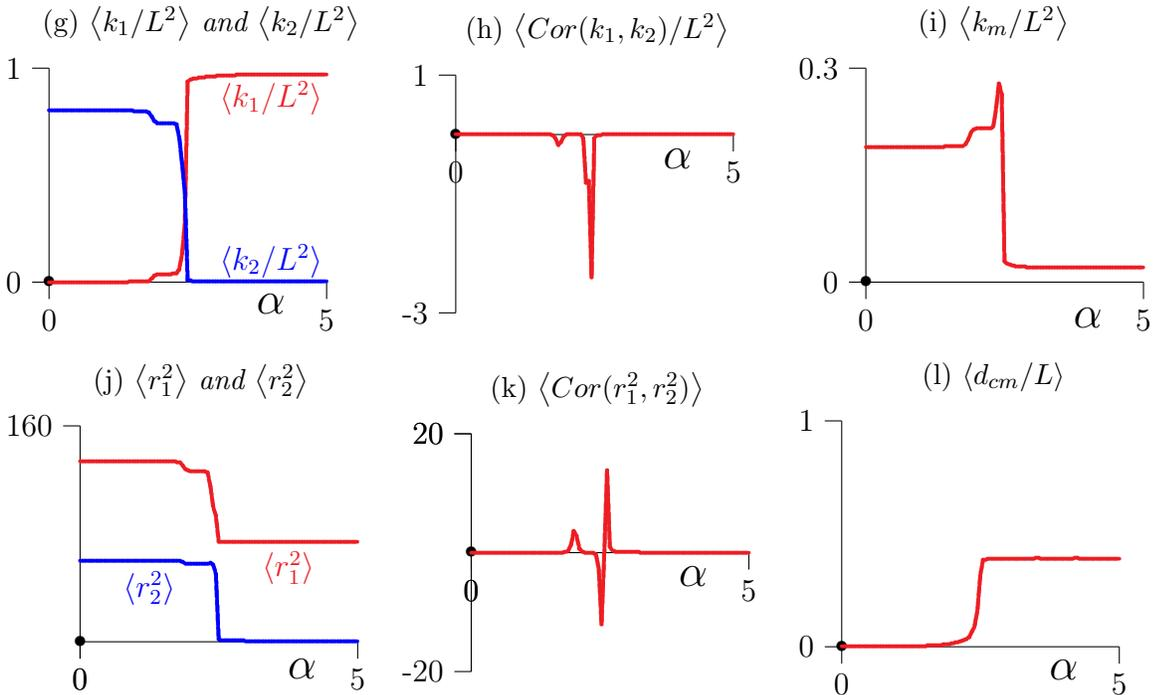


Figure 22: Across the  $\tau$  and  $\tau_1$  phase boundaries in the  $\alpha\beta$ -plane. Graphs for the unlinked model are shown in (a)-(f), and for the linked model are shown in (g)-(l). Consistent with the results in figure 10(a)-(c) and 17(a)-(c), these results show first order transitions as the  $\tau$  and  $\tau_1$  phase boundaries are crossed in the two models respectively.

Linked from  $(-2, -5)$  to  $(-2, 5)$  across  $\tau_2$ :

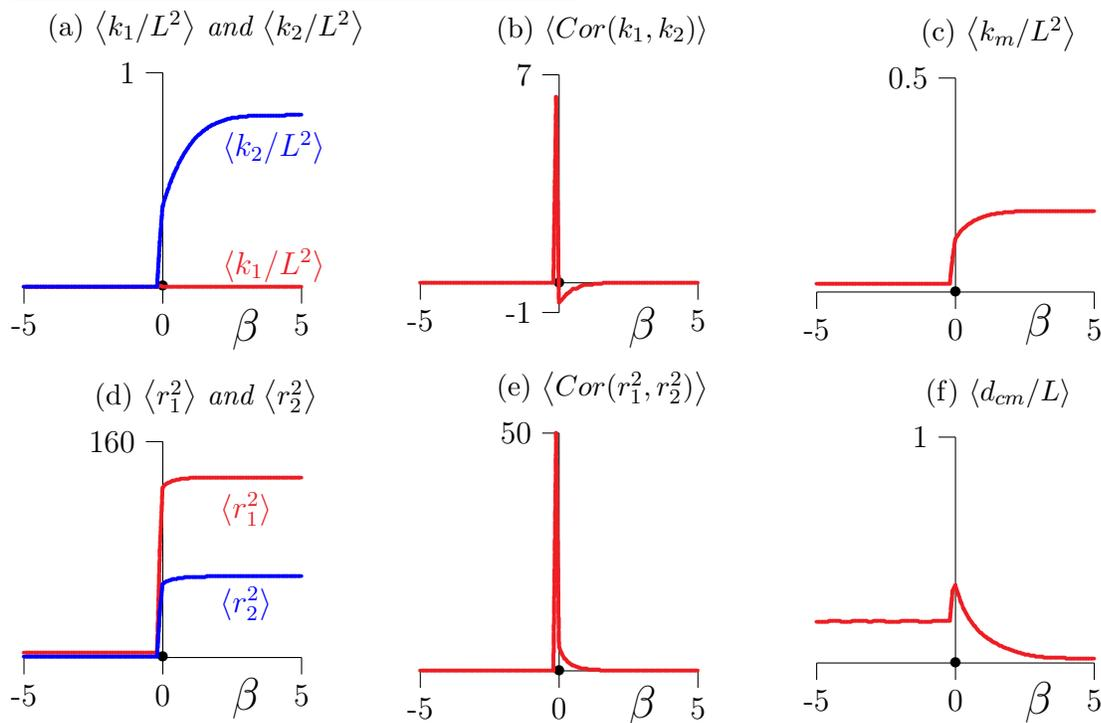
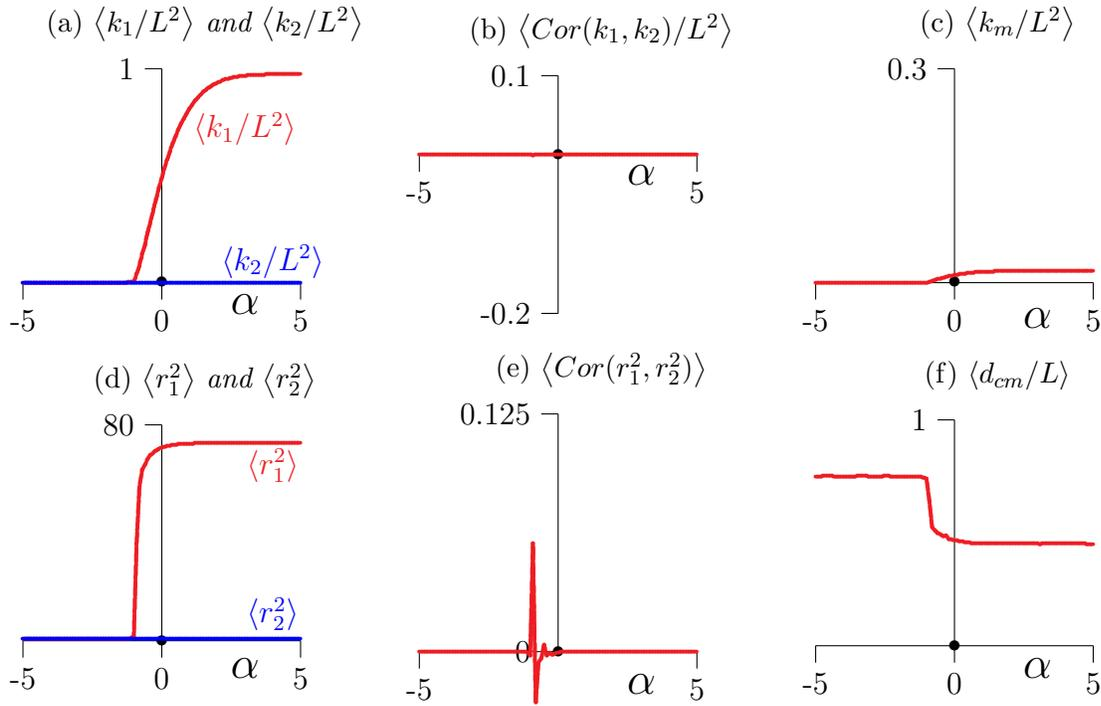


Figure 23: Across the  $\tau_2$  phase boundary in the  $\alpha\beta$ -plane (linked mode). Consistent with the results in figure 17(d)-(f), these results show a first order phase transition with sharp peaks in the correlation functions as the phase is crossed.

16. The mean number of self-contacts in the inner polygon changes discontinuously at the phase boundary, as the mean square radii of gyration of both polygons change discontinuously.

In figure 24 we show changes in the order parameters as  $\lambda_1$  (or  $\lambda_2$ ) phase boundary is crossed in the unlinked model, and the similar changes as the  $\lambda$  boundary is crossed in the linked model. Our results in the previous sections show that these are continuous phase boundaries, and the results in figure 24 are consistent with this. The mean density of self-crossings in figure 24(a) (across the  $\lambda_1$  phase boundary), and figure 24(g) (across the  $\lambda$  phase boundary) show very similar behaviour in the two models. Crossing these boundaries into the  $c_1$ -dominated phase causes the first polygon in the unlinked model, and the outside polygon in the linked model, to expand into the dense phase occupying almost all sites in the confining square. The second polygon (in the unlinked model) and the inside polygon (in the linked model) are both squeezed to minimal length by the expanding polygon, and this is consistent with the metric data reported in the figure. The mean distance between the centres-of-mass in the unlinked model decreases from the mean distance in the empty phase to a smaller distance as one polygon increases in length. In the linked model, this distance is zero in the empty phase, but becomes positive when the outer polygon expands into the  $c_1$ -dominated phase with centre-of-mass near the center of the confining square, while the inner polygon has almost minimal

Unlinked from  $(-5, -2)$  to  $(5, -2)$  across  $\lambda_1$  or  $\lambda_2$ :



Linked from  $(-5, -2)$  to  $(5, -2)$  across  $\lambda$ :

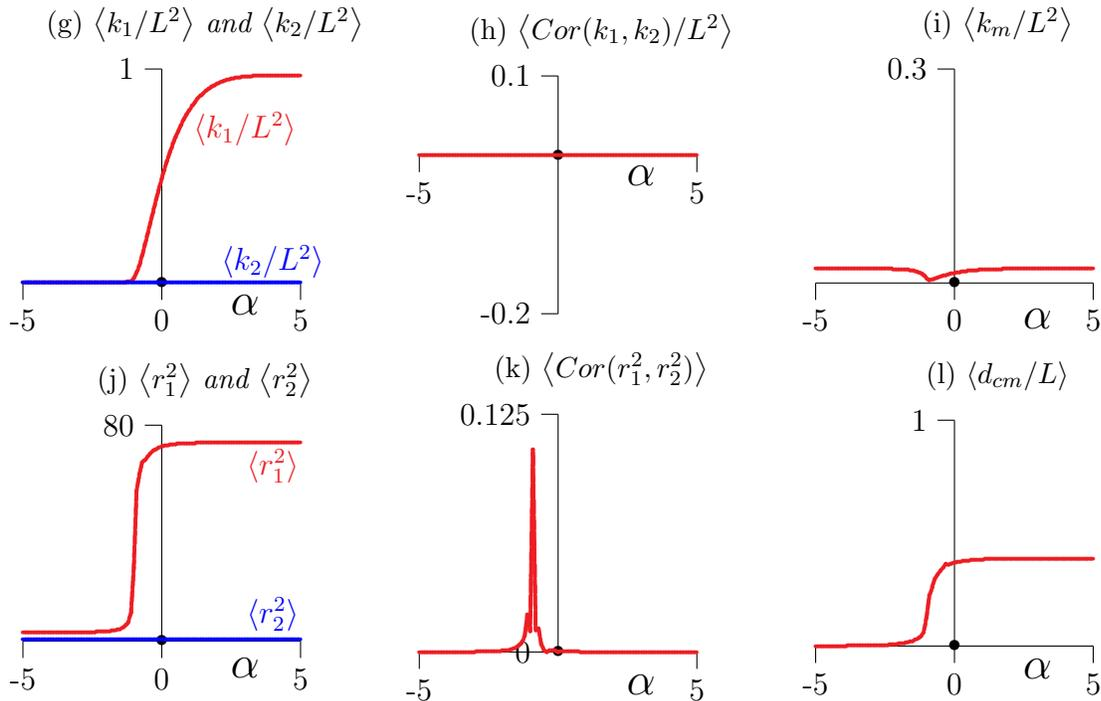


Figure 24: Across the  $\lambda_1$  (or  $\lambda_2$ ) and  $\lambda$  phase boundaries in the  $\alpha\beta$ -plane. Graphs for the unlinked model are shown in (a)-(f), and for the linked model are shown in (g)-(l). Consistent with the results in figure 11(a)-(c) and 17(g)-(i), these results show continuous transitions as these phase boundaries are crossed in the two models respectively.

length and explores the inside of the square. These observations differ from those shown in figure 23, where a first order transition is seen along the  $\tau_2$  phase boundary in the linked model.

## 5. Conclusions

We determined the phase diagrams of two square lattice models of pairs of ring polymers in the dense phase. The placements of the two polygons in a confining square were chosen in two distinct topological ways, in one case they were unlinked (or splittable) in the plane, and in the second case, linked (or unsplittable) in the plane. The phase diagrams include, in addition to an empty phase, a phase dominated by the first polygon (it is dense inside the square), and a phase dominated by the second polygon; see figures 9 and 16. These phases are separated by boundaries whose nature depends on the topology of the model. In the unlinked model, there are two lines of continuous transitions ( $\lambda_1$  and  $\lambda_2$ ) separating the empty phase from the two dense phases, while the two dense phases are separated by a line of first order transitions ( $\tau$ ). In contrast, the linked model has two curves of first order transitions ( $\tau_1$  and  $\tau_2$ ), where  $\tau_1$  separates a phase in which the outer polygon is dense from a phase in which the inner polygon is dense, and  $\tau_2$  separates the empty phase from the dense inner polygon phase. A line of continuous transitions  $\lambda$  separates the empty phase from the dense outer polygon phase.

In the case of both models we were able to determine critical exponents along the critical curves. Along the curves of first order transition the exponents are given in equations 19 (for  $\tau$ ), 32 ( $\tau_1$ ) and 35 ( $\tau_2$ ). In each case the result is consistent with the expected value  $2 - \alpha_s = 2 - \alpha'_s = 1$  reported in equation (5). We were similarly able to estimate these exponents along the lines of continuous transitions. The results are shown in table 1.

Table 1: *Estimates of  $2 - \alpha_s$  and  $2 - \alpha'_s$  across phase boundaries*

	Unlinked model			Linked model		
	$\tau$	$\lambda_1$	$\lambda_2$	$\tau_1$	$\tau_2$	$\lambda$
$2 - \alpha_s$	1.003(3)	0	0	1.02(4)	1.06(12)	0
$2 - \alpha'_s$	1.003(3)	1.55(3)	1.55(3)	1.02(4)	1.06(12)	1.57(6)

The concentration gap associated with the first order transitions may also be estimated. For example, for the critical line  $\tau$  in the unlinked model the free energy crossing  $\tau$  is given by equation (17). Taking derivatives on either side of  $\tau$  and subtracting to determine the gap gives  $H_\tau |_{\alpha=2.5} \approx 1.95$ . In the same way, by equations (27) and (29),  $H_{\tau_1} |_{\alpha=2.5} \approx 1.55$  and  $H_{\tau_2} |_{\alpha=-2.0} \approx 0.70$ .

Multicritical scaling around the multicritical points were more difficult to determine, in particular in the linked model. Our estimates of the critical exponents are less secure in the linked model. We show our best estimates in table 2.

Table 2: Estimates of  $2 - \alpha_t$  and  $2 - \alpha_u$  between  $\tau$  and  $\lambda$  boundaries

	Unlinked model		Linked model	
	$\tau$ - $\lambda_1$	$\tau$ - $\lambda_2$	$\tau_1$ - $\lambda$	$\tau_2$ - $\lambda$
$2 - \alpha_t$	1.55(3)	1.55(3)	1.57(6)	0
$2 - \alpha_u$	1.55(3)	1.55(3)	1.17(7)	0
$\phi$	1.00(4)	1.00(4)	1.3(2)	1

## Acknowledgements

EJJvR acknowledges financial support from NSERC (Canada) in the form of Discovery Grant RGPIN-2019-06303. EJJvR was also grateful to the Department of Physics and Astronomy at the University of Padova for the financial support during a visit in 2019.

## References

- [1] C Aragao de Carvalho, S Caracciolo, and J Fröhlich. Polymers and  $g\phi^4$ -theory in four dimensions. *Nucl Phys B*, 215:209–248, 1983.
- [2] M Baiesi and E Orlandini. Universal properties of knotted polymer rings. *Phys Rev E*, 86:031805, 2012.
- [3] B Berg and D Foerster. Random paths and random surfaces on a digital computer. *Phys Lett B*, 106:323–326, 1981.
- [4] S Campbell and EJ Janse van Rensburg. Parallel PERM. *J Phys A: Math Theo*, 2020.
- [5] P-G de Gennes. *Scaling Concepts in Polymer Physics*. Cornell, 1979.
- [6] P-G de Gennes. Tight knots. *Macromol*, 17:703–704, 1984.
- [7] M Delbrück. Knotting problems in biology. *Proc Symp Appl Math*, 14:55–63, 1962.
- [8] F Gassoumov and EJ Janse van Rensburg. Osmotic pressure of confined square lattice self-avoiding walks. *J Phys A: Math Theor*, 52:025004, 2018.
- [9] CJ Geyer and EA Thompson. Annealing Markov chain Monte Carlo with applications to ancestral inference. *J Amer Stat Assoc*, 90:909–920, 1995.
- [10] AY Grosberg, A Feigel, and Y Rabin. Flory-type theory of a knotted ring polymer. *Phys Rev E*, 54:6618–6622, 1996.
- [11] JM Hammersley. The number of polygons on a lattice. *Proc Camb Phil Soc*, 57:516–523, 1961.
- [12] JM Hammersley and KW Morton. Poor man’s Monte Carlo. *J Roy Stat Soc Ser B (Meth)*, 16:23–38, 1954.
- [13] JM Hammersley and DJA Welsh. Further results on the rate of convergence to the connective constant of the hypercubical lattice. *Quart J Math*, 13:108–110, 1962.
- [14] EJ Janse van Rensburg. Composite models of polygons. *J Phys A: Math Gen*, 32:4351–4372, 1999.
- [15] EJ Janse van Rensburg. The probability of knotting in lattice polygons. *Contemp Math*, 304:125–136, 2002.
- [16] EJ Janse van Rensburg. Squeezing knots. *J Stat Mech: Theo Expr*, 2007:P03001, 2007.
- [17] EJ Janse van Rensburg. Osmotic pressure of compressed lattice knots. *Phys Rev E*, 100:012501, 2019.
- [18] EJ Janse van Rensburg, E Orlandini, MC Tesi, and SG Whittington. Knot probability of polygons subjected to a force: a Monte Carlo study. *J Phys A: Math Theo*, 41:025003, 2008.
- [19] EJ Janse van Rensburg, E Orlandini, MC Tesi, and SG Whittington. Knotting in stretched polygons. *J Phys A: Math Theo*, 41:015003, 2008.

- [20] EJ Janse van Rensburg and A Rechnitzer. Generalized atmospheric sampling of knotted polygons. *J Knot Theo Ram*, 20:1145–1171, 2011.
- [21] EJ Janse van Rensburg and SG Whittington. The BFACF algorithm and knotted polygons. *J Phys A: Math Gen*, 24:5553–5567, 1991.
- [22] K Koniaris and M Muthukumar. Knottedness in ring polymers. *Phys Rev Lett*, 66:2211–2214, 1991.
- [23] ID Lawrie and S Sarlbach. Tricriticality. In C Domb and JL Lebowitz, editor, *Phase Transitions and Critical Phenomena*, volume 9, pages 65–161. Academic Press, 1984.
- [24] N Madras. Critical behaviour of self-avoiding walks that cross a square. *J Phys A: Math Gen*, 28:1535–1547, 1995.
- [25] Maple 17. Waterloo Maple, Inc.
- [26] R Matthews, AA Louis, and JM Yeomans. Confinement of knotted polymers in a slit. *Mol Phys*, 109:1289–1295, 2011.
- [27] N Metropolis, AW Rosenbluth, MN Rosenbluth, AH Teller, and E Teller. Equation of state calculations by fast computing machines. *J Chem Phys*, 21:1087–1092, 1953.
- [28] JPJ Michels and FW Wiegel. Probability of knots in a polymer ring. *Phys Lett A*, 90:381–384, 1982.
- [29] E Orlandini, AL Stella, and C Vanderzande. Loose, flat knots in collapsed polymers. *J Stat Phys*, 115:681–700, 2004.
- [30] A Rechnitzer and EJ Janse van Rensburg. Generalized atmospheric Rosenbluth methods (GARM). *J Phys A: Math Theo*, 41:442002, 2008.
- [31] VV Rybenkov, NR Cozzarelli, and AV Vologodskii. Probability of DNA knotting and the effective diameter of the DNA double helix. *Proc Nat Acad Sci*, 90:5307–5311, 1993.
- [32] SY Shaw and JC Wang. Knotting of a DNA chain during ring closure. *Science*, 260:533–536, 1993.
- [33] MC Tesi, EJ Janse van Rensburg, E Orlandini, DW Sumners, and SG Whittington. Knotting and supercoiling in circular DNA: a model incorporating the effect of added salt. *Phys Rev E*, 49:868–872, 1994.
- [34] MC Tesi, EJ Janse van Rensburg, E Orlandini, and SG Whittington. Monte Carlo study of the interacting self-avoiding walk model in three dimensions. *J Stat Phys*, 82:155–181, 1996.
- [35] C Vanderzande. On knots in a model for the adsorption of ring polymers. *J Phys A: Math Gen*, 28:3681–3700, 1995.